NASA/CR-1998-208719

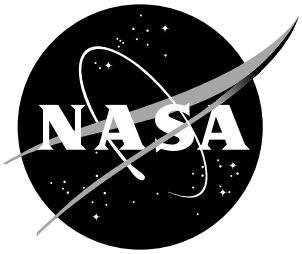

Stereo-Video Data Reduction of Wake Vortices and Trailing Aircrafts

Rachel Alter-Gartenberg
Computer Sciences Corporation, Hampton, Virginia

September 1998

The NASA STI Program Office ... in Profile

Since its founding, NASA has been dedicated to the advancement of aeronautics and space science. The NASA Scientific and Technical Information (STI) Program Office plays a key part in helping NASA maintain this important role.

The NASA STI Program Office is operated by Langley Research Center, the lead center for NASA's scientific and technical information. The NASA STI Program Office provides access to the NASA STI Database, the largest collection of aeronautical and space science STI in the world. The Program Office is also NASA's institutional mechanism for disseminating the results of its research and development activities. These results are published by NASA in the NASA STI Report Series, which includes the following report types:

- TECHNICAL PUBLICATION. Reports of completed research or a major significant phase of research that present the results of NASA programs and include extensive data or theoretical analysis. Includes compilations of significant scientific and technical data and information deemed to be of continuing reference value. NASA counterpart of peer-reviewed formal professional papers, but having less stringent limitations on manuscript length and extent of graphic presentations.

- TECHNICAL MEMORANDUM. Scientific and technical findings that are preliminary or of specialized interest, e.g., quick release reports, working papers, and bibliographies that contain minimal annotation. Does not contain extensive analysis.

- CONTRACTOR REPORT. Scientific and technical findings by NASA-sponsored contractors and grantees.

- CONFERENCE PUBLICATION. Collected papers from scientific and technical conferences, symposia, seminars, or other meetings sponsored or co-sponsored by NASA.

- SPECIAL PUBLICATION. Scientific, technical, or historical information from NASA programs, projects, and missions, often concerned with subjects having substantial public interest.

- TECHNICAL TRANSLATION. English-language translations of foreign scientific and technical material pertinent to NASA's mission.

Specialized services that complement the STI Program Office's diverse offerings include creating custom thesauri, building customized databases, organizing and publishing research results ... even providing videos.

For more information about the NASA STI Program Office, see the following:

- Access the NASA STI Program Home Page at ***http://www.sti.nasa.gov***

- E-mail your question via the Internet to help@sti.nasa.gov

- Fax your question to the NASA STI Help Desk at (301) 621-0134

- Phone the NASA STI Help Desk at (301) 621-0390

- Write to:
  NASA STI Help Desk
  NASA Center for AeroSpace Information
  7121 Standard Drive
  Hanover, MD 21076-1320

NASA/CR-1998-208719

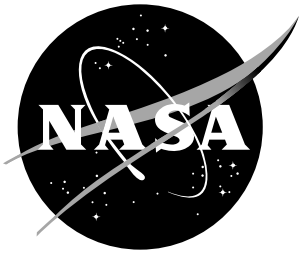

Stereo-Video Data Reduction of Wake Vortices and Trailing Aircrafts

Rachel Alter-Gartenberg
Computer Sciences Corporation, Hampton, Virginia

National Aeronautics and
Space Administration

Langley Research Center
Hampton, Virginia 23681-2199

Prepared for Langley Research Center
under Contract NAS1-20431

September 1998

Available from:

NASA Center for AeroSpace Information (CASI)
7121 Standard Drive
Hanover, MD 21076-1320
(301) 621-0390

National Technical Information Service (NTIS)
5285 Port Royal Road
Springfield, VA 22161-2171
(703) 605-6000

Contents

STEREO-VIDEO DATA REDUCTION OF WAKE VORTICES AND TRAILING AIRCRAFTS

Rachel Alter-Gartenberg
Computer Sciences Corporation, 3217 N. Armistead Ave., Hampton, VA 23666.

Abstract

This report presents stereo image theory and the corresponding image processing software developed to analyze stereo imaging data acquired for the wake-vortex hazard flight experiment conducted at NASA Langley Research Center. In this experiment, a leading Lockheed C-130 was equipped with wing-tip smokers to visualize its wing vortices, while a trailing Boeing 737 flew into the wake vortices of the leading airplane. A Rockwell OV-10A airplane, fitted with video cameras under its wings, flew at 400 to 1000 feet above and parallel to the wakes, and photographed the wake interception process for the purpose of determining the three-dimensional location of the trailing aircraft relative to the wake. The report establishes the image-processing tools developed to analyze the video flight-test data, identifies sources of potential inaccuracies, and assesses the quality of the resultant set of stereo data reduction.

1 INTRODUCTION

Knowledge of wake-vortex effects on trailing airplanes is necessary for high volume air-traffic control, terminal area productivity, and the prevention of flight accidents. The Vehicle Performance Branch of the Flight Dynamics and Control Division at NASA Langley Research Center conducted a series of flight experiments in which a trailing Boeing 737 flew into the wake of a leading C-130 whose wing-tip vortices were visualized by smoke emission. An OV-10A airplane, with two cameras mounted under its wings, flew at 400–1000 feet above the trailing airplane, and photographed its interaction with the wake-vortices. Imaging of the same event from two different locations enables the extraction of depth information and object location in space (3D) through stereo techniques. In the context of the image processing tools and the data reduction techniques, "trailing" and "intercepting" refer to the same airplane, which trails the leading wake-generating airplane, and flies into its wakes.

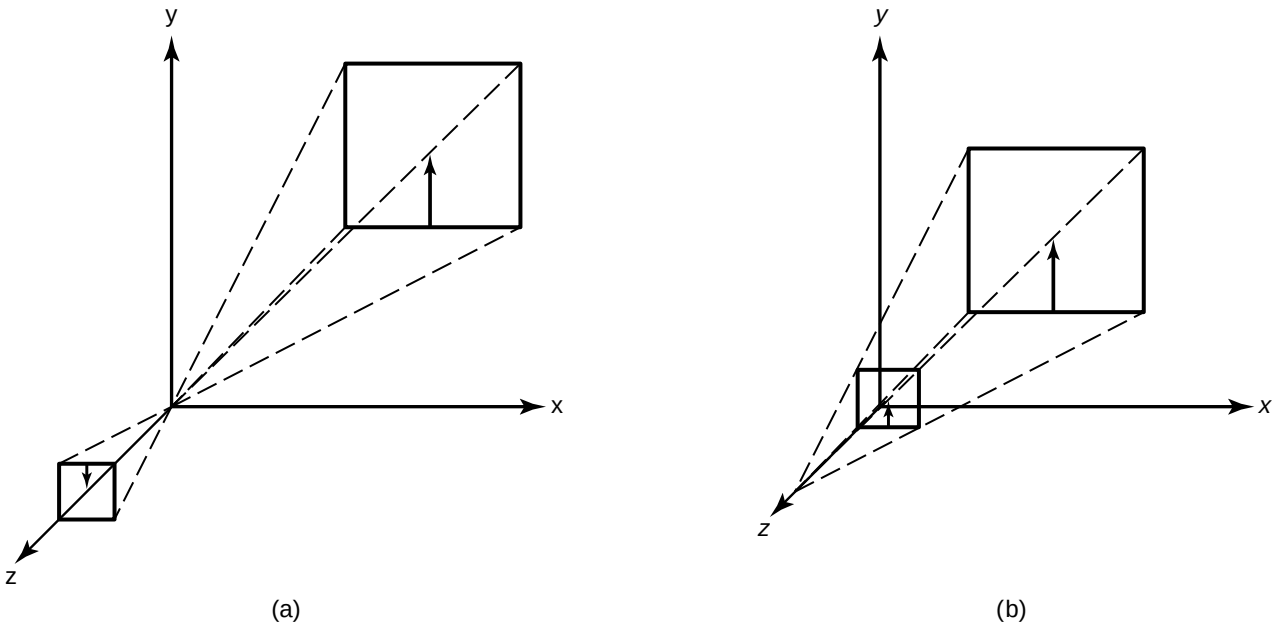

Figure 1: Geometrical model of pinhole camera.

Computer Sciences Corporation (CSC) has developed a PV-Wave based image processing software package that extracts 3D information from stereo video images for the purpose of determining the three-dimensional location of the trailing aircraft relative to the wake. This Contractor Report (CR) describes the software package, including the mathematical and image processing tools. Section 2 sets the theory of image formation in general and the geometry of stereo imaging in particular. Section 3 describes the experimental set-up. Section 4 discusses the software package developed at CSC, while Section 5 describes the data reduction process and analyzes the results.

2 THE THEORY OF STEREO IMAGING

2.1 Image Formation

An image is formed by projecting a set of 3D object points into a 2D image plane in a perspective mapping [1]–[4]. The transformation can be carried out by the eye, camera, video recorder, or any other imaging device. Figure 1 illustrates a simple "pinhole camera" model, where the image plane is located at the focal point f of the lens. According to this model, rays of light pass through the center of the lens, and the

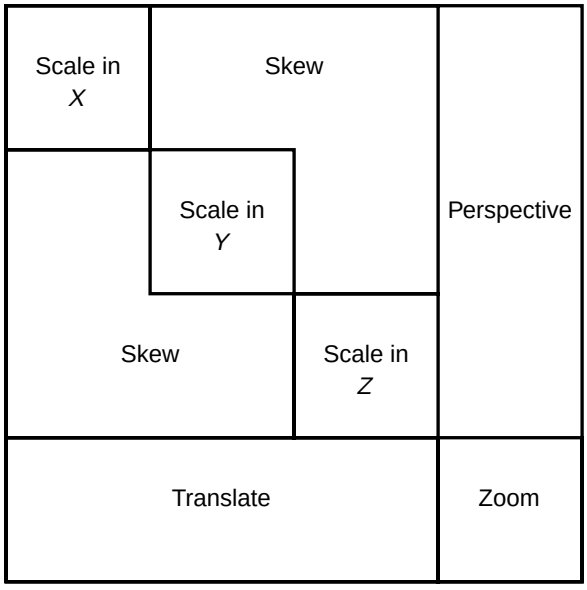

Figure 2: The 4-by-4 homogeneous transformation matrix. (From [2], p. 481)

image of the object is formed on an image-plane at a distance f. The image plane in Fig. 1(a) is placed behind the focal point (the point of projection), and the imaged-object is inverted. It is therefore more convenient and intuitive to place the focal point behind the image plane, and get the imaged object erect, as illustrated in Fig. 1(b). In the former arrangement, the focal point is at $z = 0$, and the image plane is at $+f$ on the z-axis, while in the latter set-up, the focal point is at $+f$ on the z-axis, and the image plane is at $z = 0$.

This transformation is a projective-perspective mapping, since its dimensions retain similarity to the original object (perspective), and the dimensionality is reduced from 3 to 2 (projection). Using homogeneous coordinates and a 4-by-4 matrix formulation (Fig. 2) to unify the representation and calculation of geometrical transformations [2], the perspective transformation of an object point $P_o = (x_o, y_o, z_o, 1)$ into the image point $P_i = (x_i, y_i, z_i, w_i)$ is performed by the following homogeneous transformation:

$$\begin{pmatrix} x_i \\ y_i \\ z_i \\ w_i \end{pmatrix} = \begin{pmatrix} f & 0 & 0 & 0 \\ 0 & f & 0 & 0 \\ 0 & 0 & f & 0 \\ 0 & 0 & 1 & f \end{pmatrix} \begin{pmatrix} x_o \\ y_o \\ z_o \\ 1 \end{pmatrix} = \begin{pmatrix} fx_o \\ fy_o \\ fz_o \\ z_o + f \end{pmatrix}, \tag{1}$$

where w is an arbitrary constant, and the viewpoint is at $+f$ along the z-axis. The same homogeneous

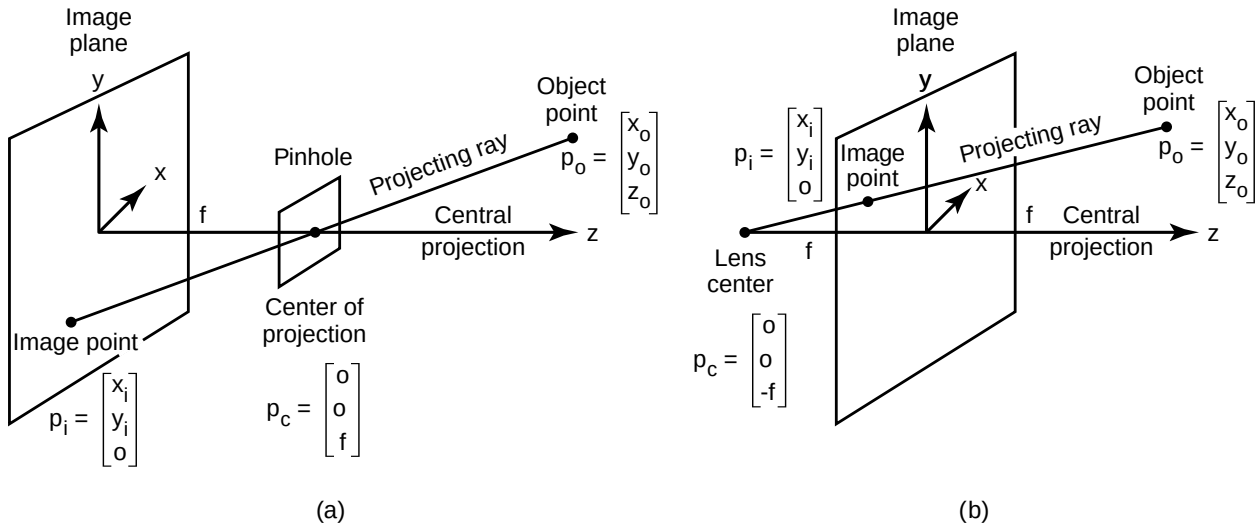

Figure 3: Image projection model.

transformation for a viewpoint at $-f$ along the z-axis is given by

$$\begin{pmatrix} x_i \\ y_i \\ z_i \\ w_i \end{pmatrix} = \begin{pmatrix} -f & 0 & 0 & 0 \\ 0 & -f & 0 & 0 \\ 0 & 0 & -f & 0 \\ 0 & 0 & 1 & -f \end{pmatrix} \begin{pmatrix} x_o \\ y_o \\ z_o \\ 1 \end{pmatrix} = \begin{pmatrix} -fx_o \\ -fy_o \\ -fz_o \\ z_o - f \end{pmatrix}. \tag{2}$$

Returning to physical coordinates, we divide by the fourth component, and get

$$P_i = \begin{pmatrix} x_i \\ y_i \\ z_i \end{pmatrix} = \begin{pmatrix} fx_o/(z_o + f) \\ fy_o/(z_o + f) \\ fz_o/(z_o + f) \end{pmatrix},$$

and

$$P_i = \begin{pmatrix} x_i \\ y_i \\ z_i \end{pmatrix} = \begin{pmatrix} fx_o/(f - z_o) \\ fy_o/(f - z_o) \\ fz_o/(f - z_o) \end{pmatrix},$$

for the $+f$ and $-f$ cases, respectively. The first and second components can be derived using similar triangles, while the third component is a parameter proportional to the distance along the projecting ray from the center of the lens to the center of the object point [1], as illustrated in Fig. 3.

Knowledge of the camera's focal length, the photograph scale, and the object's position in the image plane, allows a 3D reconstruction of the object via an inverse perspective, assuming that the line of sight

intersects the physical plane at only one point ([2], Appendix 1). This approach has been successfully applied to depth extraction from images obtained from a similar set of flight tests. In their data reduction, Childers and Snow [5] assumed that the trailing airplane and wake vortices of the forward airplane are at the same altitude. Therefore, the distance from the trailing airplane to the wake vortices was extracted directly from the image, and the calibration factor was set as the ratio between the imaged and actual wing-span of the trailing airplane. When this is not the case, then using stereo imaging to extract depth information from two synchronized images of the same object is a more accurate approach.

2.2 Stereo Imaging

2.2.1 Binocular Vision

The positioning of the human eye enables the acquisition of a similar scene from two nearby points at the same horizontal level [4]. Objects separated by depth will differ in their positioning in the images formed by each eye. Disparity (location difference) creates the sensation of depth. Human disparity is measured in minutes of arc, where one minute of disparity corresponds roughly to a difference of 2.5cm for an object 2.5m away. A person with normal eyesight senses the strongest stereo fusion at an approximate distance of 50 cm in front of the eye [1]. For eyes separated by $d = 5$ cm, the stereo angle is $5.72°$.

It is therefore inferred that for a strong stereo sensation, the ratio of $d/f = 1/10$ must be maintained while creating stereo pairs from a single view of the object with a scaled separation d between the viewer's eyes and a focal length f. Such a process entails a horizontal translation of $d/2 = \pm f/20$ for the left and right images respectively, followed by their appropriate perspective projection transformations, as given by the homogeneous transformation matrices

$$L = \begin{pmatrix} 1 & 0 & 0 & 0 \\ 0 & 1 & 0 & 0 \\ 0 & 0 & 1 & -1/f \\ f/20 & 0 & 0 & 1 \end{pmatrix} \qquad R = \begin{pmatrix} 1 & 0 & 0 & 0 \\ 0 & 1 & 0 & 0 \\ 0 & 0 & 1 & -1/f \\ -f/20 & 0 & 0 & 1 \end{pmatrix}. \tag{3}$$

The resulting shifted representations, when viewed through a stereoscope, are blended into a single 3D view of the scene, as it would appear to the eye.

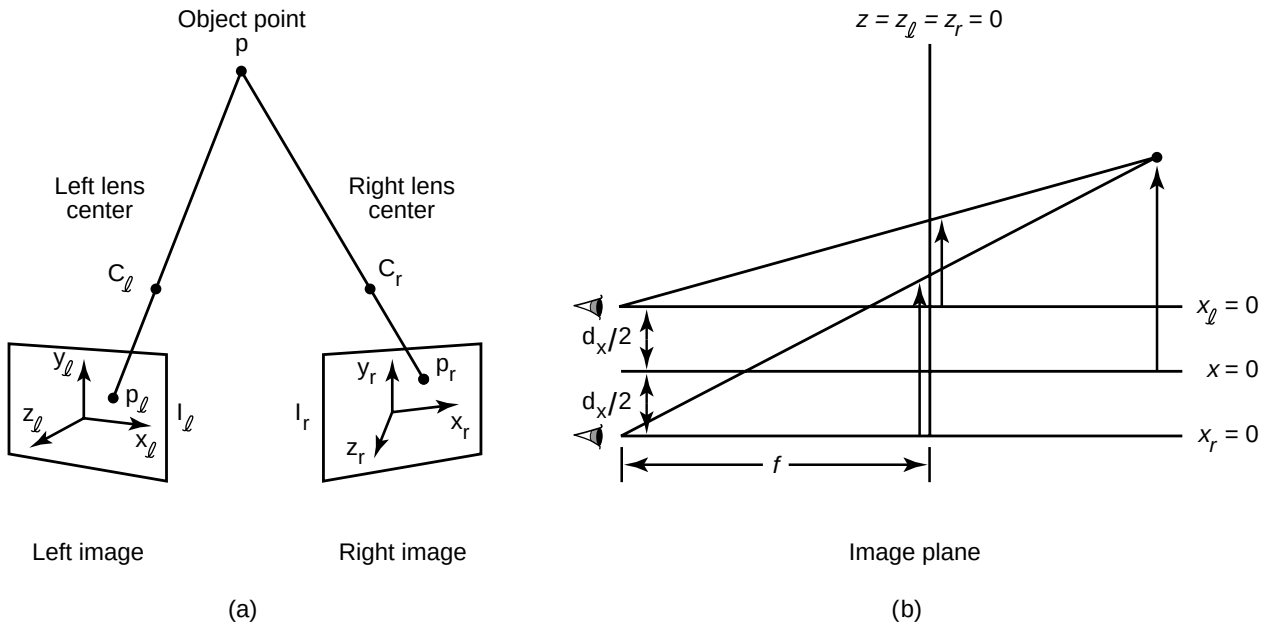

Figure 4: Binocular imaging system.

2.2.2 Parallel Stereo Mapping

The accuracy of depth extraction from stereo pairs depends on a proper time and spatial synchronization of the stereo images. Therefore, the process is most useful for the extraction of the 3D positioning of a limited and well defined set of object points. The stereo data reduction scheme employed for the wake-vortex experiment is based on the matching of the trailing airplane's nose, tail and wing-tips, and their corresponding nearest wake vortices locations (i.e., Figures 5 and 6 top, and Figure 9).

Figure 4 illustrates the basic binocular geometry, assuming that the two cameras are aimed in parallel in the z-direction. Using the previous analysis, depth can be extracted using the disparity information alone. For this procedure we assume that P_l and P_r are the projections of a point P on the left and right images respectively. The images are acquired by two cameras with the same focal length f, located at a distance d apart on the xy-plane with no disparity in the z-direction. Using a different coordinate system for each camera, centered on the respective focal point, the point P is represented by (x_l, y_l, z_l) in the left-camera coordinate system and by (x_r, y_r, z_r) in the right-camera coordinate system, where

$$x_l - x_r = d_x, \qquad y_l - y_r = d_y, \qquad z_l = z_r. \tag{4}$$

The coordinates of the object point P in space are (x_o, y_o, z_o), and the coordinates of P_l and P_r on the left

and right image-planes are (x_{il}, y_{il}) and (x_{ir}, y_{ir}) respectively. Assuming the geometry of Fig. 3(b), P lies on the line

$$x_l = -\frac{x_{il}(z_l - f)}{f}, \qquad y_l = -\frac{y_{il}(z_l - f)}{f}$$

in the left camera system, and on the line

$$x_r = -\frac{x_{ir}(z_r - f)}{f}, \qquad y_r = -\frac{y_{ir}(z_r - f)}{f}$$

in the right camera system. Translating the right-camera line to the left camera coordinate system, we get

$$x_l = d_x - \frac{x_{ir}(z_r - f)}{f}, \qquad y_l = d_y - \frac{y_{ir}(z_r - f)}{f}$$

from which we can extract the depth

$$z_l = f\left(1 + \frac{d_x}{x_{ir} - x_{il}}\right) = f\left(1 + \frac{d_y}{y_{ir} - y_{il}}\right) \tag{5}$$

of the point P from the left camera, assuming no disparity in the z-direction. Generally, depth information can be extracted from disparity along either the x-axis or the y-axis. Therefore, the set of x_{ir}, x_{il}, d_x and f are sufficient to extract z_l or z_r. Likewise, x_l and y_l can be extracted by

$$x_l = -Ax_{il}, \qquad y_l = -Ay_{il}, \tag{6}$$

where $A = (z_l - f)/f$.

2.2.3 Compensation for Non-Parallel Imaging

When the two cameras do not aim in parallel along the z-direction, but converge at an angle θ, then this angle must also be accounted for in the extraction of the depth information. Assuming no disparity in the z-direction, the coordinate system relative to the left camera is set such that the camera aim is parallel in the z-direction. The right camera is then rotated by an angle θ in the z-direction measured positive in the counterclockwise direction. As before, the two cameras have the same focal length f and are translated relative to each other by d_x and d_y in the x- and y-directions, respectively. The image formation transformation given in Eq. 1 changes for the right camera as follows:

$$\begin{pmatrix} x_{ir} \\ y_{ir} \\ z_{ir} \\ w_{ir} \end{pmatrix} = \begin{pmatrix} f\cos\theta & -f\cos\theta & 0 & f(d_y\sin\theta - d_x\cos\theta) \\ f\sin\theta & f\cos\theta & 0 & -f(d_x\sin\theta + d_y\cos\theta) \\ 0 & 0 & f & 0 \\ 0 & 0 & 1 & f \end{pmatrix} \begin{pmatrix} x_o \\ y_o \\ z_o \\ 1 \end{pmatrix} \tag{7}$$

$$= \begin{pmatrix} fx_o\cos\theta - fy_o\sin\theta + f(d_y\sin\theta - d_x\cos\theta) \\ fy_o\sin\theta + fy_o\cos\theta - f(d_x\sin\theta + d_y\cos\theta) \\ fz_o \\ (z_o + f) \end{pmatrix}.$$

Returning to physical coordinates, we divide by the fourth component, and get

$$P_i = \begin{pmatrix} x_{ir} \\ y_{ir} \\ z_{ir} \end{pmatrix} = \begin{pmatrix} f(x_o\cos\theta - y_o\sin\theta - d_x\cos\theta + d_y\sin\theta)/(z_o + f) \\ f(y_o\sin\theta + y_o\cos\theta - d_x\sin\theta - d_y\cos\theta)/(z_o + f) \\ fz_o/(z_o + f) \end{pmatrix},$$

where the new coordinates (x_{ir}, y_{ir}, z_{ir}) should be substituted in Eqs. 5 and 6.

3 EXPERIMENTAL SET-UP

The experimental set-up and pre-test procedures are detailed in [6, 7]. Generally speaking, the leading C-130 was equipped with wing-tip smokers to visualize its vortex cores. A photographing OV-10A airplane, with cameras mounted under its wings, flew at approximately 500 to 1000 feet above and parallel to the two wakes. The OV-10A airplane surveyed the trailing Boeing 737 intercepting the leading C-130's wake vortices, with two miniature (lipstick-size) Elmo VHS video cameras mounted vertically through "peepholes" on the bottom of the wingtip fairings (see Figs. 6 and 9 in Ref. [7])

3.1 Analysis

The assumption of parallel downward viewing of the cameras holds true only on the ground. Airplane deflection caused by the aerodynamic load, and the subsequent rotation angle of the image planes during flight, disputes this assumption, and should be taken into account as a source of inaccuracy. The stereo process assumes a wing deflection of about 10° for the trailing Boeing 737 and about 2° for the OV-10A.

Preliminary studies [6] indicate that at 12,000 feet, the stereo effects were minimal, i.e., Earth images at 12,000 feet from both cameras were identical, with disparity (parallax) smaller than a pixel. However, the current analysis shows that the theoretical disparity at 12,000 feet is about 2 pixels, and the stereo pair becomes identical only at about 48,000 feet. For objects that are 500 to 1000 feet away from the cameras, as is the case with this data reduction process, the disparity is between 50 to 26 pixels respectively.

Accurate stereo reduction is contingent upon zero z-direction disparity between the two image-planes as given by the conditions on z_l and z_r in Eq. 4. In this experimental set-up, data reduction is made relative to the OV-10's left image plane. Roll angles cause the image plane depth location to shift. Furthermore, changes in the roll-angle or pitch-attitude shift the field-of-view. Data reduction of flight 558 experiment showed, for example, roll angles that ranged between $-1.11°$ and $6.3°$. No adjustment relative to a fixed inertial coordinate system has been made, and at present, the stereo data reduction software does not compensate for non-parallel stereo imaging.

3.2 Data Recording

A time code, accurate within one millisecond, was superimposed on each of the "left" and "right" video cassette recording. For each flight-test, the relevant 'time windows of interest' for analysis were determined. These sequences were digitized using the Video Image Processing System (VIPS) at Langley's Data Visualization and Animation Laboratory (DVAL). The VIPS is a hardware/software combination built around the DataCube Inc.'s MaxVideo 200 modular image processing subsystem, interfaced to a Motorola MVME 167-33MB computer. The real-time digital disk is capable of storing up to 19 minutes of full-frame digitized 8-bit images. The software interface is the ImageFlow Image Processing software from DataCube Inc., running under LynxOS. The colored video information was digitized by an 8-bit black and white A/D converter, using the green channel. The gain and offset were adjusted so that on one hand the recorded image had a good signal-to-noise ratio, and on the other hand, the digitized image was neither saturated nor under exposed.

Accurate stereo reduction depends largely on accurate time-synchronization of the stereo pairs. Every effort has been made to synchronize the right and left video frames, by finding the transitional frame of the required time-window on both the left and right sequences of the digitized data. Pairs of synchronized frames (time-wise) were saved with a time resolution of $4/15$ of a second (every eighth frame).

3.3 Calibration

The cameras mounted on the wing-tips of the OV-10A airplane were calibrated at Langley in terms of the cameras' parameters and geometrical distortion, using analytical photogrammetric techniques [5]. For each camera, these parameters were incorporated into two 4-by-4 transformation matrices which account for the camera distortion and allow polynomial warping of each frame prior to processing. Empirical evidence showed that images acquired by the left camera are rotated by about $\theta = 2°$ clockwise relative to the

right camera. The rotation was probably caused by the span-wise wing deflection under aerodynamic load. Although the actual deflection and wing-tip rotation were never measured or calculated, the rotation was estimated to be around 2°–3°, in agreement with the experimental observation. Therefore, the left frame was rotated 1° clockwise, and the right frame was rotated 1° counterclockwise, so that the resulting image planes aim in parallel along the z-direction.

Photogrammetric calculations determined the cameras' nominal focal length to be $f = 0.0245$ feet (8.5mm), and set the feet/pixel ratio to $F = 4.095E-5$. The distance between the cameras on the ground was measured as $d_x = 39.06$ feet and $d_y = 0$ feet. This distance was adjusted to $39.06\cos(3°) = 39.00$ feet to account for in-flight deflection. The substitution of these values in Eq. 5 shows a theoretical disparity of about two and a half pixels for stereo frames acquired at a distance of 10,000 feet, about two pixels at a distance of 20,000 feet, and less than half a pixel at images acquired at a distance of 48,000 feet.

4 THE SOFTWARE PACKAGE

4.1 Image Processing Tools

The data reduction software is based on Visual Numerics' PV-Wave 6.10 software package, and can be run on any platform that has access to a PV-Wave license. The following Image Processing (IP) tools were used in this process:

- **Pre-processing**
  Image warping using the photogrammetric parameters of the cameras, followed by $-1°$ and $1°$ rotations for the left and right frames to compensate for the image-plane in-flight rotation, precedes the data reduction process. When the Geosynchronous Positioning System (GPS) data is available, the software extracts the altitudes of both the photographing OV-10A and the trailing Boeing 737, and calculates their relative distance. Additionally, when the orientation files are available, the software extracts the pitch, roll and true-heading angles of the OV-10 and the trailing Boeing 737 at the video time.

- **Background and object statistical analysis**
  Background statistics are obtained by averaging a large background portion of each frame. The time code bar is masked with the statistical background level, to avoid false detection near the bar. The threshold intensity for objects of interest, such as the trailing airplane and the wakes, is set as a

trade-off between the background statistics, the strength of the water reflection signal, the difference in illumination between the left and right images, and the objects' intensity. For the flight 558 data reduction process, the object threshold ranged between 130 and 150 for the left frame, and between 100 and 150 for the right frame. For flight 559, where the airplane was brighter than the wakes, thresholds were set between 75 and 110 for the wakes and between 90 and 140 for the airplane, depending on the time sequence. For flight 560, these values ranged between 120-160 for the airplane, and 110-160 for the wakes. In general, as a result of the Sun angle and orientation relative to the image planes during image acquisition, left frames were brighter than right frames in all of these experiments.

- **Noise reduction**

  The experiments were carried out over the Atlantic Ocean. Therefore, some stereo frames contain substantial water-reflection signal that is wide enough to be detected as a wake signal, and bright enough to be detected as an airplane signal. A threshold operator, which sets all image elements with intensity below a pre-set object intensity to the calculated constant background level, reduces background noise, minimizes the detection of water reflection as wake image elements, and increases the image signal-to-noise ratio.

- **Image filtering**

  This analysis requires only the silhouette of the objects, not their inner details. Therefore, the nonlinear median filter, known for its ability to preserve sharp transitions and remove "salt and pepper" noise, was chosen to filter the airplane image from the wakes and water reflection signal in each frame. Effectively, this filtering separates each thresholded image frame into two images, one that contains only wake elements, and the other that contains only the trailing airplane image. The airplane image is extracted from the thresholded frame by using the median filter with a width of 11-17 pixels, which is about 3 times wider than the image of the wake, but still small relative to the airplane's width. Similarly, the wake image is extracted from the original frame by masking the airplane image from the median-filtered image, and filtering the result with a median filter, using the wake's width as a parameter.

  Figure 5 illustrates an example of the image filtering process, executed on flight-test 558, conducted in the 332rd day of 1995, at 15:18:44 hour (GMT). This pair illustrates data reduction for high signal-to-noise ratio, where the threshold for the signal (airplane and wakes) was set to 140 and 130, for the left and right frames respectively, while the background threshold level was estimated at 65, and the median width was set to 11 pixels. The first row illustrates the original stereo pair.

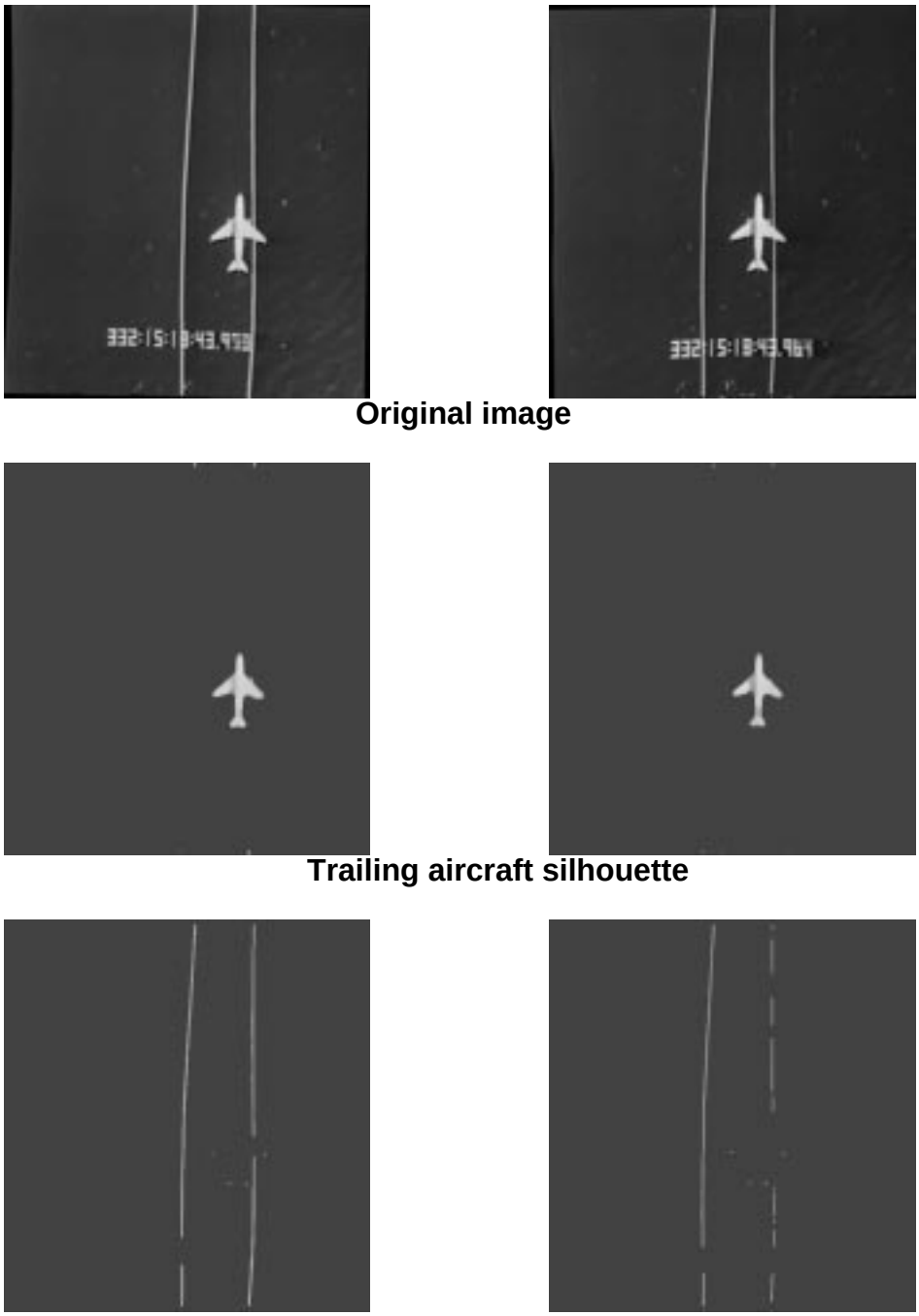

Figure 5: Separation of the trailing airplane image from the image of the wakes for high signal-to-noise ratio

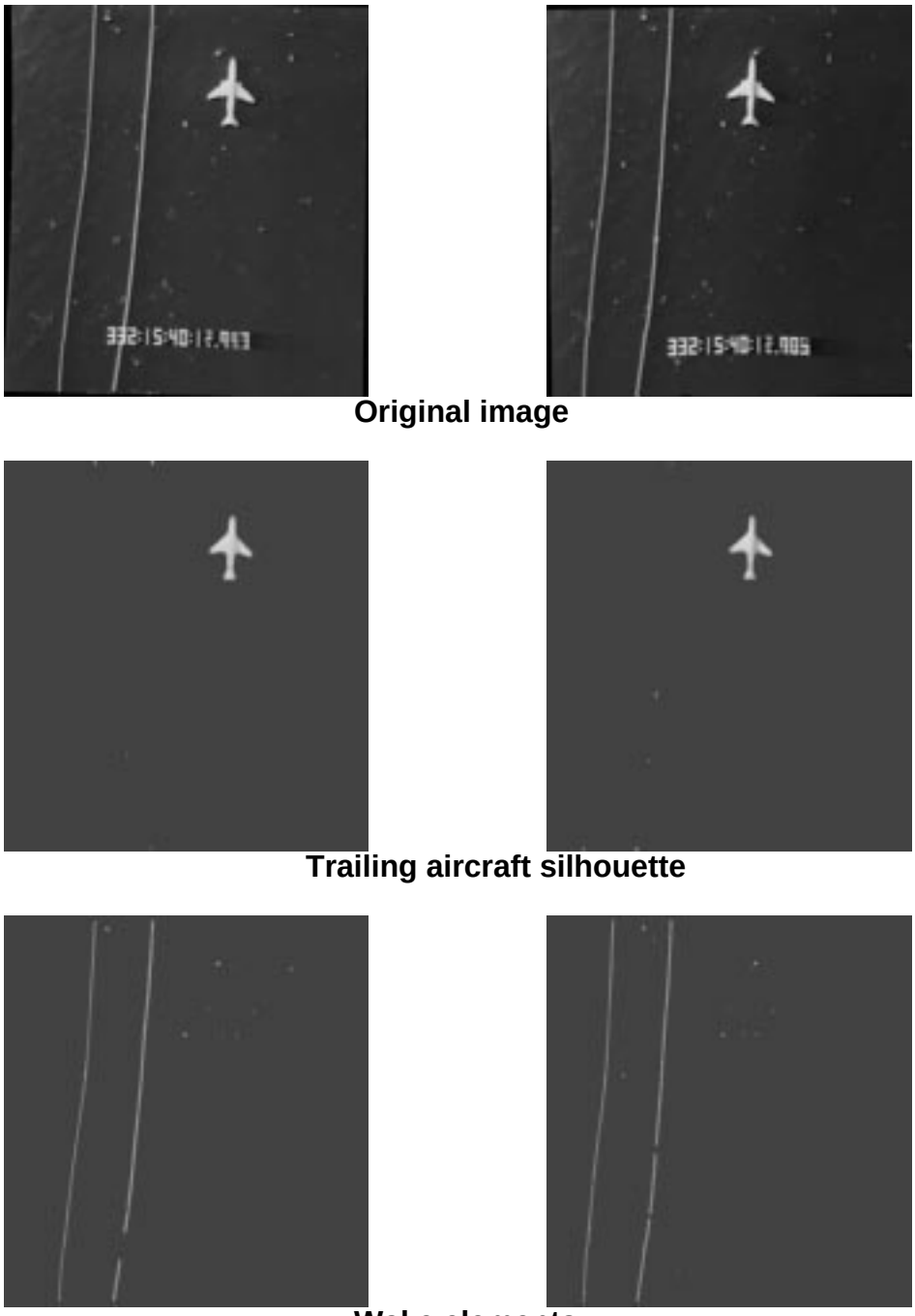

Figure 6: Separation of the trailing airplane image from the image of the wakes for low signal-to-noise ratio

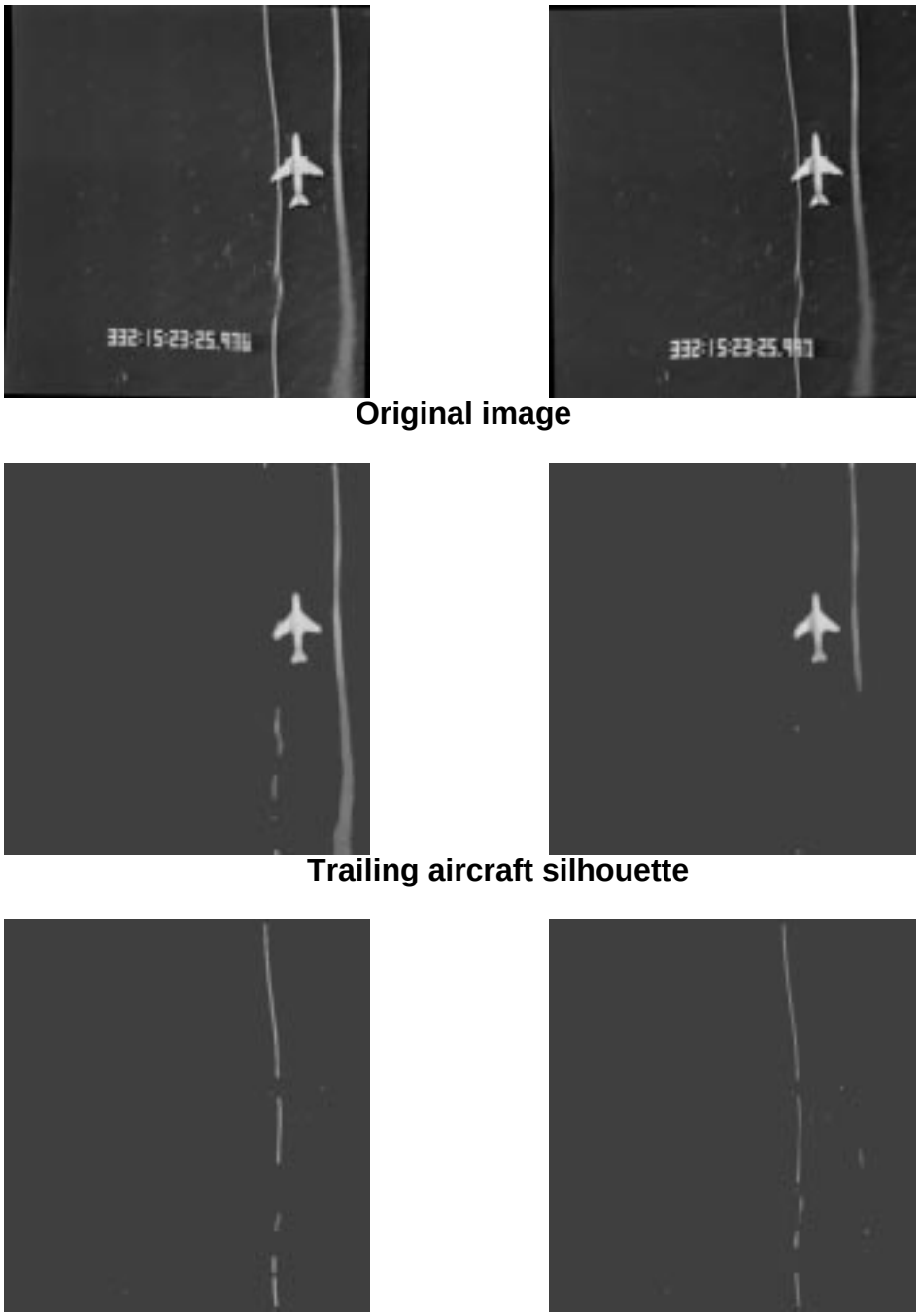

Figure 7: Separation of the trailing airplane image from the image of the wakes for unlocalized wake and a median of width 11.

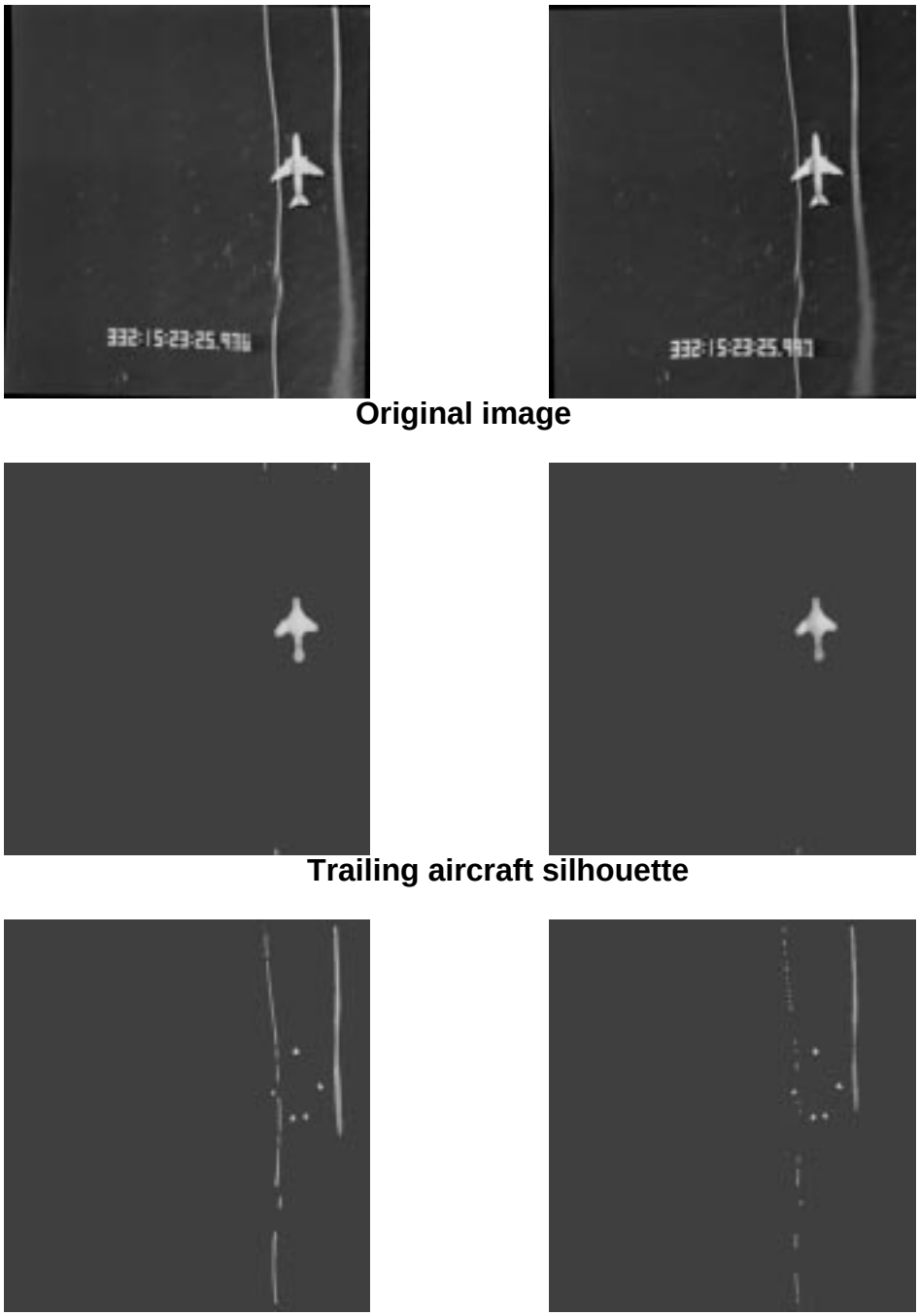

Figure 8: Separation of the trailing airplane image from the image of the wakes for unlocalized wake and a median of width 17.

The second and third rows illustrate the extracted and filtered trailing airplane silhouette, and the wake elements respectively. Figure 6 demonstrates separation for a low signal-to-noise ratio case, caused by extensive water reflection noise. Data reduction was conducted on the same flight test, at 15:40:12 hours. The threshold for the background was determined as 66, and the threshold for the signal was set to 100 for both the left and right frames. This low threshold was necessary to retain the wake information. Higher thresholds wash out the wake information. However, this set has a strong signal of water reflection residuals that are as wide and bright as the wakes. Figs. 7 and 8 illustrate a case of unlocalized and weak wake signal, when the right wake begins to dissipate, starting around 15:23:26 hours. Threshold for the airplane image was set to 140 and 120, for the left and right frames respectively, while the background threshold level was estimated at 64. When the width of the median filter was set, as before, to 11 pixels, the process was unable to separate the trailing airplane from the wake (Fig. 7). However, when the width of the median filter was set to 17 pixels to account for the right wake characteristics, the two objects were properly separated (Fig. 8). A wider median causes inaccurate tip localization, as the detected tip is localized too much into the wing, and is not close enough to the true edge.

These examples show that a complete separation of the airplane image from the wake signal is not always attainable. As a result, tip location extraction is prone to false detection, when the process mistakes wake elements as airplane elements. Methods that reduce the probability of false or inaccurate detection are detailed in Section 4.2. Figure 9 illustrates the final detected tips superimposed on the original stereo pairs illustrated in Figs. 5 and 6 respectively. This figure clearly demonstrates the robustness of the data reduction process to false detection.

4.2 Wake Extraction

Wake information is extracted at the center of the image plane, and at the image-plane y-location of each extracted airplane's tip. Wake locations are extracted from the wake-frames pair by finding the "center-of-mass" of the two wakes on both frames. A strong water reflection signal might result in a strong and false wake candidate. When more than two equally strong wake candidates are detected, the first two maximum strength centers are chosen as the x wake location at the y-location of interest. This detection is later checked against previously detected wake locations, using a referenced wake location list. When a wake is covered by or too close to the airplane, it is typically filtered out of the wake image, as illustrated by the third row in Fig. 6. The process can then extract only one wake location and uses a referenced list

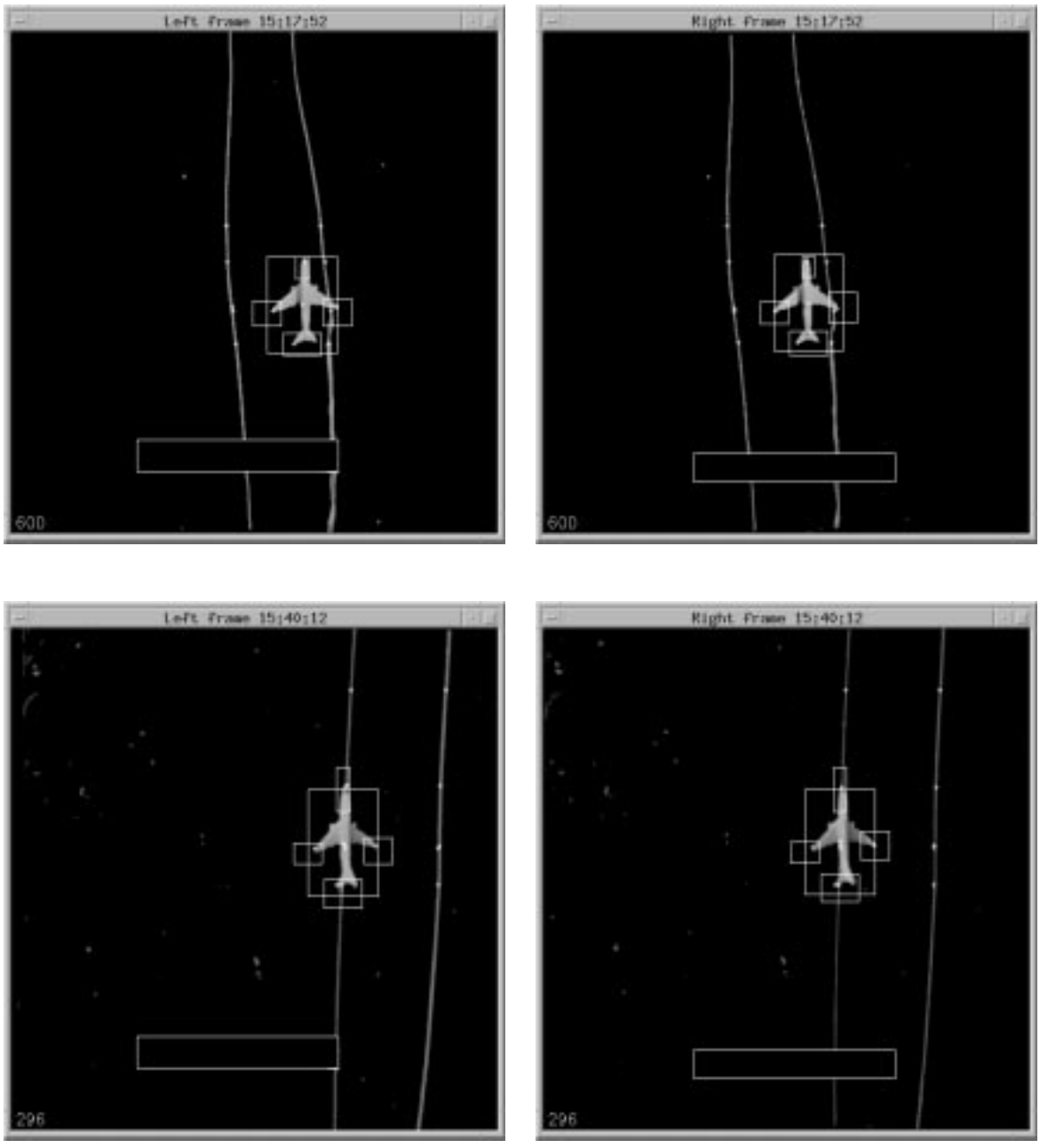

(a) Left **(b) Right**

Figure 9: Final data reduction for the stereo pairs illustrated in Figs. 5 and 6.

of previously extracted wake information to estimate the missing wake location, as illustrated in the final extraction result, shown in the second row of Fig. 9. Wake information extracted close to the airplane's tip allows the assessment of both the distance between the extracted tip and the wake, and the influence of the trailing plane on the wake's behavior. Final tip detection is illustrated by the "+" sign in Fig. 9.

Additionally, the wake extraction process includes the extraction of the wake orientation along the image plane relative to the sampling lattice. By extracting the wake location at the top, center, and bottom of the captured frame, the orientation of the wake is calculated as the wake's slope. Figure 10 illustrates stereo pairs with wakes orientation that is not parallel to the image frame. The sequence of the wake x-location relative to the left camera is further assessed for the general behavior of the wake as a function of time, as illustrated in Fig. 11.

The referenced wake location list summarized the four wake locations, from the left and right wakes in the left and right frames, respectively. The list is initiated by extracting the wake information as close as possible to the center of the image plane, either before the trailing airplane's nose, or after its tail. The process is performed as the first data reduction operation for all the separated wake frames, even when the trailing airplane does not appear in the stereo pair. The preliminary wake extraction process ensures the extraction of at least one accurate pair of wake locations from each frame. This location is saved on the referenced list, and is later updated to wake locations closer to the tip-search sub-images. For example, after extracting the nose-tip, the reference wake list is updated to a location in front of the airplane, just before the nose. Likewise, after the tail-tip search, the referenced wakes are updated at a location just after the tail location. The update process insures a more accurate location extraction in cases where the wake is close to the trailing airplane, is completely covered by it, or when the wake x-location within the frame changes rapidly. The right wing-tip smoker malfunctioned in flights 560 and 561. Modified software which assumes only one wake, and does not use the referenced wake location list, has been used to accommodate a one-wing-tip smoker situation.

Errors in determining the wake location are monitored to dismiss airplane elements or water reflection elements detected as wake elements, and to account for regions where the wake information is covered or missing altogether. To minimize false detection, features that are extracted from the airplane frame with a width smaller than the estimated wake's width are eliminated. The set of detected wakes differ by a common uniform shift that reflects the dynamics of the wakes as a function of time. When an extracted wake location does not differ by that common uniform shift, the extracted location is replaced by the appropriate reference wake location, after taking into account the general uniform shift for all new locations relative to the reference wake location list. This exchange process, therefore, accounts for shifts

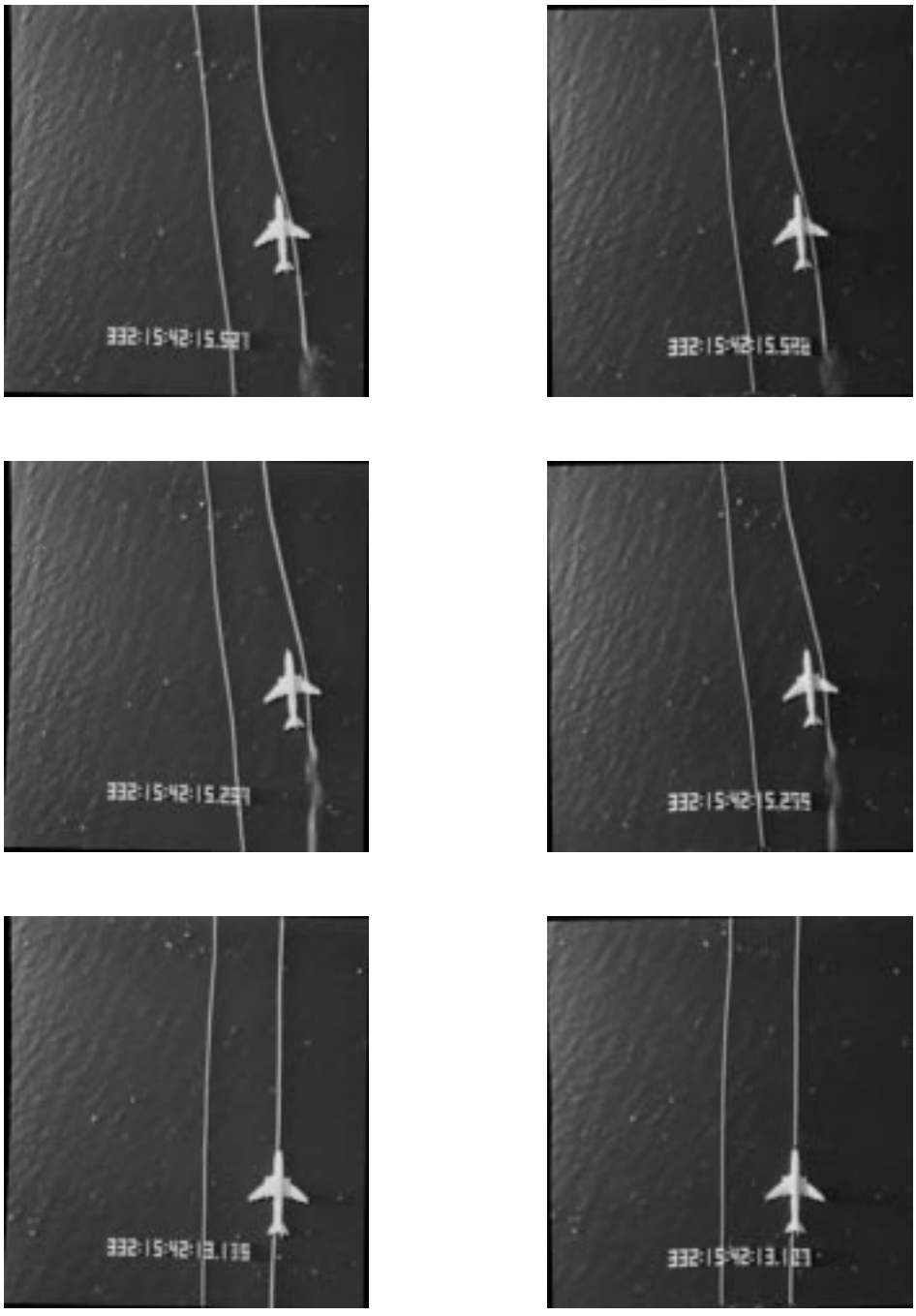

(a) Left **(b) Right**

Figure 10: Stereo pairs with different wakes orientations.

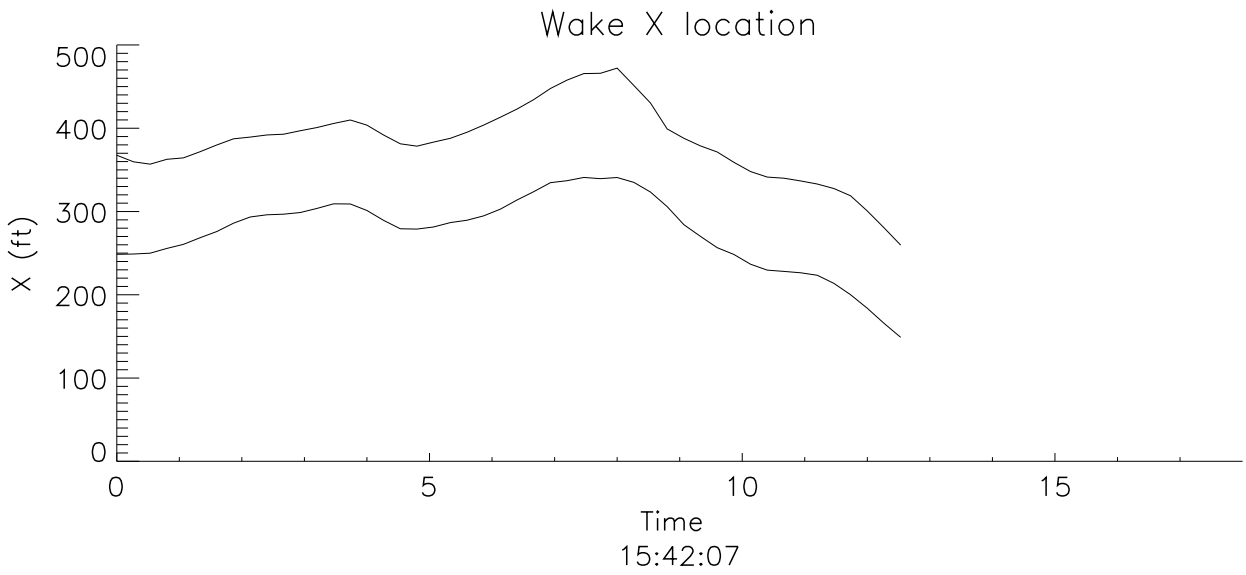

Figure 11: The X-component of the wake location after stereo reduction.

due to wake orientation across the image plane.

4.3 Airplane Extraction

Having separated the wake signal from the airplane signal, and having saved them in two separate files, the software determines whether the stereo pair has actually captured the trailing airplane. The software proceeds to determine its location within the image plane only for stereo frames which contain the airplane. The process estimates the airplane "center-of-mass", its wing span, and its body length. These parameters determine the airplane's location within the image frame, as illustrated in Fig. 9, and serve to eliminate false airplane detection, which may occur when the estimated airplane's width is close to the wake's width.

Having determined the airplane location within the image plane, the search process extracts the approximate location of the airplane's four tips: the two wing-tips, the nose, and the tail, and sets up a search sub-image around each one, as illustrated in Fig. 9. The search for each tip location is conducted within its appropriate search sub-image on the thresholded image plane, and not on the separated filtered airplane signal, to ensure a better tip detection. The search direction for each tip is conducted from the outside towards the objects. Hence, the search for the nose tip location is conducted from top to bottom, whereas the search for the right wing tip is conducted from right to left. A tip location is determined by the first object element along the search direction that is not an object element in the wake image.

5 DATA ANALYSIS

5.1 Data Reduction

Although individual attention to each stereo pair could have resulted in a more accurate stereo data reduction, there are too many paired frames for an efficient interactive process. Therefore, stereo data reduction is conducted sequentially with no interactive interaction. Inaccuracies occur for detected pairs for which $y_r - y_l$ is too large, bearing in mind the assumption of $d_y = 0$. Targeted points for stereo reduction that are too close to the border of one frame and vanish from the other are eliminated from further processing. Similarly, targeted points for stereo reduction that are covered by the time-code bar or a wake, and can be extracted from only one of the two frames, are also eliminated from further processing.

Results are summarized in three files, in a Comma Separated Value (csv) format, to allow further analysis, processing, and data manipulation. The first output file contains wake information extracted from the center of each image-plane. Each record of this file contains the video time, the left and right wake (x, y, z) locations, and their general imaged orientation. An example of such a file is illustrated in Table 1, where LL stands for Left-frame Left-wake, LR for Left-frame Right-wake, etc. The second output file summarizes the trailing airplane's stereo data reduction. In addition to the video time, each record of this file contains the four airplane-tip (x, y, z) locations and their corresponding wake (x, y, z) locations relative to the left image plane, as detailed in Section 4.2. Finally the airplane's stereo data reduction file contains an estimate for the measured Boeing 737 wing span, which is one of the means by which the overall accuracy of the reduction process is assessed. Excerpts from such a file are illustrated in Tables 2 and 3, for the nose and left wing data reductions, respectively. The structure of these two output files enables the inspection of false detection. For example, if one of the four detected Boeing 737 tips differs substantially in depth from the others, or does not belong to the 2D plane formed by the detected tips, it is a likely false detection. These files also enable easy extraction of additional geometrical information, such as the wake separation at different image plane locations.

The third file summarizes flight information collected by outside recorders at time references that are relevant to the analysis of the extracted stereo data. Each record of this file contains the video time of the stereo pair, and data collected from GPS files and camera angle recorders from both the OV-10A and Boeing 737 airplane as close to the video time as possible. Data from the OV-10A and Boeing 737 GPS files include the airplanes' altitude in meters, and the difference in altitude between the two airplanes in feet, as illustrated in Table 4. The process accounts for the 10 seconds difference between GPS time and actual time. Data extracted from the OV-10A and Boeing 737 orientation files include the (θ, ϕ, ψ) angles

time 15:42:57+	y-location (pixels)	Left Wake Location (feet)	Right Wake Location (feet)	LL (deg)	LR (deg)	RL (deg)	RR (deg)
0.00	141	170.689,161.525,685.405	269.208,161.525,685.405	-89.2	-86.7	-88.6	90.0
0.27	141	162.670,161.525,685.405	274.993,166.412,706.143	-87.5	90.0	89.7	-88.6
0.53	141	158.088,161.525,685.405	268.062,161.525,685.405	89.5	79.5	88.6	81.5
0.80	141	151.352,156.916,665.851	264.866,156.916,665.851	89.6	-82.9	-71.4	-84.3
1.07	141	154.690,156.916,665.851	278.372,161.525,685.405	89.6	90.0	87.8	89.5
1.33	141	160.255,156.916,665.851	282.954,161.525,685.405	89.2	-88.4	88.4	87.8
1.60	141	161.220,152.563,647.381	278.220,156.916,665.851	89.6	87.1	88.4	86.5
1.87	141	164.466,152.563,647.381	282.672,156.916,665.851	89.5	88.4	88.4	87.3
2.13	141	160.027,148.446,629.909	284.897,156.916,665.851	89.5	88.6	88.4	87.8
2.40	141	152.745,144.544,613.354	270.503,152.563,647.381	90.0	87.8	88.9	86.7
2.67	141	145.570,144.544,613.354	252.673,148.446,629.909	-89.2	85.1	89.6	83.9
2.93	141	135.318,144.544,613.354	240.907,144.544,613.354	-88.4	86.7	89.6	87.5
3.20	141	122.863,140.843,597.648	239.882,144.544,613.354	90.0	90.0	90.0	90.0
3.47	141	111.875,140.843,597.648	224.749,140.843,597.648	-89.2	-60.9	56.6	30.1
3.73	190	106.333,200.033,629.909	220.405,194.776,613.354	-88.8	76.0	70.9	45.3
4.00	190	92.5247,185.049,582.726	201.775,189.788,597.648	-88.4	-87.1	-89.6	-88.0
4.27	190	85.5197,180.542,568.531	191.944,180.542,568.531	-88.0	-85.9	-89.6	-87.1
4.53	190	82.6690,180.542,568.531	186.452,176.248,555.011	-87.1	-86.3	-88.4	-88.0
4.80	190	81.7188,180.542,568.531	191.944,180.542,568.531	-87.1	-86.7	-88.4	-88.0
5.07	190	86.4699,180.542,568.531	195.745,180.542,568.531	-86.7	-87.1	-87.5	-88.4
5.33	190	89.3205,180.542,568.531	197.645,180.542,568.531	-86.3	-88.0	-87.5	-88.8
5.60	190	89.6029,185.049,582.726	196.737,185.049,582.726	-87.8	90.0	-88.8	89.2
5.87	190	85.9041,189.788,597.648	191.867,185.049,582.726	-89.2	-89.8	90.0	89.2

Table 1: Wake information file for flight 558, time window 15:42:57 hours

time 15:42:57+	Nose Location (feet)	Left Wake @ Nose Location (feet)	Right Wake @ Nose Location (feet)
0.00	N/A	N/A	N/A
0.27	N/A	N/A	N/A
0.53	N/A	N/A	N/A
0.80	N/A	N/A	N/A
1.07	N/A	N/A	N/A
1.33	N/A	N/A	N/A
1.60	N/A	N/A	N/A
1.87	N/A	N/A	N/A
2.13	N/A	N/A	N/A
2.40	N/A	N/A	N/A
2.67	N/A	N/A	N/A
2.93	N/A	N/A	N/A
3.20	N/A	N/A	N/A
3.47	N/A	N/A	N/A
3.73	N/A	N/A	N/A
4.00	N/A	N/A	N/A
4.27	N/A	N/A	N/A
4.53	N/A	N/A	N/A
4.80	N/A	N/A	N/A
5.07	188.463, 0.906074, 542.120	90.6074, 0.906074, 542.120	188.463, 0.906074, 542.120
5.33	188.463, 2.71822, 542.120	90.6074, 2.71822, 542.120	187.557, 2.71822, 542.120
5.60	190.162, 3.71048, 555.011	89.0516, 3.71048, 555.011	184.839, 3.62429, 542.120
5.87	182.121, 2.71822, 542.120	80.7030, 2.78286, 555.011	189.094, 2.85066, 568.531

Table 2: Part of the airplane's data reduction file for flight 558, time window 15:42:57 hours, which shows the nose 3D location, and the wake location adjacent to the nose.

time 15:42:57+	Left Wing Location (feet)	Left Wake @ Left Wing Location (feet)	Left Wake @ Left Wing Location (feet)
0.00	201.086, 44.2179, 629.909	165.819, 46.7410, 665.851	267.091, 46.7410, 665.851
0.27	192.726, 39.9804, 613.354	153.645, 42.1984, 647.381	257.518, 42.1984, 647.381
0.53	196.875, 37.9010, 629.909	148.235, 38.9524, 647.381	264.866, 40.0637, 665.851
0.80	198.980, 34.7426, 629.909	147.153, 35.7063, 647.381	257.518, 35.7063, 647.381
1.07	204.244, 30.5314, 629.909	146.340, 30.5314, 629.909	260.764, 31.3783, 647.381
1.33	211.614, 25.2673, 629.909	154.727, 25.9683, 647.381	262.929, 25.9683, 647.381
1.60	217.931, 22.1089, 629.909	151.720, 21.5279, 613.354	262.149, 22.1089, 629.909
1.87	218.354, 20.5027, 613.354	158.974, 21.0561, 629.909	274.831, 21.6402, 647.381
2.13	219.379, 24.6033, 613.354	156.846, 24.6033, 613.354	267.413, 25.2673, 629.909
2.40	210.765, 25.9710, 597.648	152.745, 26.6536, 613.354	264.254, 27.3730, 629.909
2.67	199.659, 25.3226, 582.726	140.843, 25.9710, 597.648	250.133, 26.6536, 613.354
2.93	196.780, 25.9710, 597.648	131.853, 25.9710, 597.648	240.907, 26.6536, 613.354
3.20	186.023, 23.3747, 582.726	117.847, 23.3747, 582.726	231.741, 23.9732, 597.648
3.47	179.206, 24.3486, 582.726	109.082, 24.3486, 582.726	223.750, 24.9721, 597.648
3.73	169.139, 31.3572, 568.531	101.290, 32.1402, 582.726	220.405, 33.8295, 613.354
4.00	161.406, 41.7430, 555.011	90.9069, 41.7430, 555.011	202.774, 44.9498, 597.648
4.27	161.537, 56.0629, 568.531	86.0770, 53.4583, 542.120	186.651, 53.4583, 542.120
4.53	155.840, 63.0782, 555.011	83.3588, 61.6130, 542.120	190.162, 63.0782, 555.011
4.80	155.840, 71.4268, 555.011	85.3411, 71.4268, 555.011	192.018, 71.4268, 555.011
5.07	159.551, 74.2097, 555.011	87.8892, 72.4859, 542.120	194.800, 74.2097, 555.011
5.33	N/A	N/A	N/A
5.60	N/A	N/A	N/A
5.87	N/A	N/A	N/A

Table 3: Part of the airplane's data reduction file for flight 558, time window 15:42:57 hours, which shows the left wing 3D location, and the wake location adjacent to that wing.

video time 15:42:57+	GPS time	OV10 altitude (m)	B737 altitude (m)	difference (feet)
0.00	15:43:07	1744.44	1542.50	662.53
0.53	15:43:08	1739.10	1539.16	655.97
1.60	15:43:09	1732.74	1536.20	644.82
2.67	15:43:10	1725.81	1533.58	630.69
3.73	15:43:11	1719.07	1531.51	615.37
4.53	15:43:12	1714.09	1530.41	602.62
5.60	15:43:13	1711.00	1529.27	596.22

Table 4: The relevant GPS data for flight 558, time window 15:42:57 hours.

that correspond to the true heading, roll, and pitch angles of each airplane respectively. GPS data is used to assess the accuracy of the depth extraction, as illustrated in Figs. 15, 16 and 17. Extracted angles are not incorporated in the current data reduction process.

The data reduction process is accompanied by graphical tools for visual inspection of the data reduction process accuracy. Each video pair is illustrated side by side on the console. Results from different stages of the data reduction process appear on the screen as appropriate. For example, when the time bar code is filtered out from each frame, its location is marked on the displayed frame. When the process detects the airplane, its sub-image location, together with its corresponding tip search sub-areas, are marked on the displayed frame. All detected stereo pairs, which are candidates for stereo reduction, are also marked on the displayed frames, as illustrated in Fig. 9. Consequently, while the process is not interactive, the detection accuracy can be assessed by inspection.

The accuracy of the extracted data is graphically compared to known features of this experiment. For example, the calculated wing span is compared to the known span of the Boeing 737. The measured depth between detected points on the Boeing 737 image and the cameras is compared to the difference in altitude measured from the GPS files. Finally, the wakes' x-location relative to the left canmera's image plane is plotted as a function of time, assuming a constant depth. These visual aids contribute to the quality assurance process and to the frame-by-frame accuracy determination.

Parallax error in pixels	Depth perturbation from true depth of 1000	900	800	700	600	500 in feet	Displacement for true depth of 1000	900	800	700	600	500 in feet
4.0	206.8	164.1	127.1	95.4	68.8	46.9	8.1	7.1	6.2	5.3	4.5	3.6
3.5	176.4	140.4	109.7	82.1	59.3	40.5	6.9	6.1	5.3	4.6	3.9	3.2
3.0	147.5	117.7	91.7	69.2	50.1	34.3	5.8	5.1	4.5	3.9	3.3	2.7
2.5	120.0	96.0	75.0	56.7	41.2	28.3	4.7	4.2	3.7	3.2	2.7	2.2
2.0	93.7	75.2	58.9	44.7	32.5	22.4	3.7	3.3	2.9	2.5	2.1	1.7
1.5	68.7	55.3	43.4	33.0	24.1	16.6	2.7	2.4	2.1	1.8	1.6	1.3
1.0	44.8	36.1	28.4	21.6	15.8	10.9	1.7	1.6	1.4	1.2	1.0	0.9
0.5	21.9	17.7	14.0	10.7	7.8	5.4	0.9	0.8	0.7	0.6	0.5	0.4

Table 5: Stereo reduction sensitivity to inaccurate parallax detection.

5.2 Error Analysis

For a given true depth-value in feet, the corresponding true parallax in pixels can computed by using Eq. 5. Adding perturbations to the calculated parallax, which corresponds to inaccurate tip detection, the same equation can calculate the depth extraction as a function of the perturbed parallax data. The difference between the latter and the initial depth denotes the depth perturbation. Depth perturbation as a function of parallax perturbations, as illustrated in Fig. 12, indicates the sensitivity of depth measurements to inaccurate tip location detection. Likewise, the same perturbation in the parallax measurement can be translated into error in the X or Y location extraction, by using Eq. 6, as illustrated in Fig. 13. Table 5 summarizes the sensitivity of the data reduction techniques (in feet) to perturbations in parallax data (in pixels).

As an example, error analysis shows that for a difference in altitude of 500 feet between the trailing Boeing 737 and the OV10, an error of ± 2 pixels in detecting the true parallax of any given stereo pair, corresponds to an error of about ± 22 feet in the depth extraction and about ± 2 feet in the extraction of X. Likewise, for a difference in altitude of 1000 feet between the trailing Boeing 737 and the OV10, an error of ± 2 pixels in detecting the true parallax of any given extracted point corresponds to an error of ± 94 feet for the depth calculations, and 4 feet for the X placement.

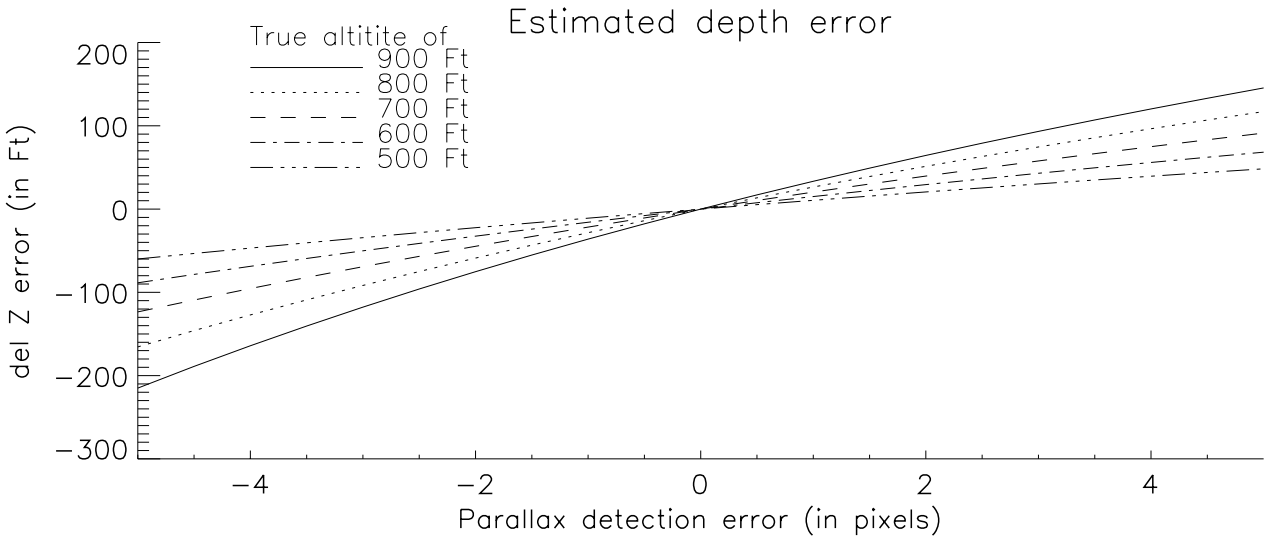

Figure 12: Sensitivity of depth extraction as function of error in the parallax detection for Flight 558

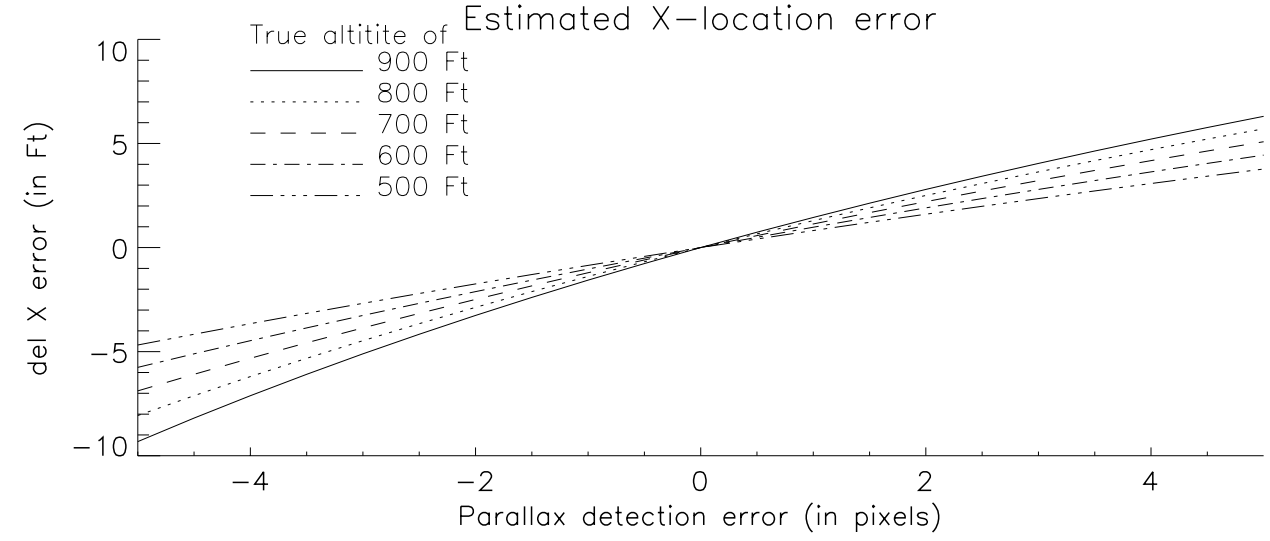

Figure 13: Sensitivity of X-location extraction as function of error in the parallax detection for Flight 558

5.3 Results

The median filter, combined with the masking and thresholding operation, causes at least 1-2 pixel error in detecting the airplane tips, i.e., tips are typically extracted 1-2 pixels into the object instead of at their true edge. The assumption of a general parallax error of two pixels corresponds to about 2-4 feet error in the X location and 20-100 feet error in the depth extraction for a range of 500-1000 feet difference in altitude between the trailing Boeing 737 and the OV10.

Figures 14–25 illustrate the extracted data for time windows of 15:17:52, 15:42:57, 16:01:10 and 16:02:11 hours respectively, of flight 558. The 15:17:52 case demonstrates the capture of the trailing aircraft from a distance of about 900 feet. A detection error of only one pixel translates, in this case, to an error in depth measurement of about 36 feet, and an X displacement error of about 2 feet. The 15:42:57 case indicates that the airplane's nose is out of the frame. Therefore, wakes can be measured only after the encounter, where the right wake begins to dissipate, is unlocalized and spreads apart. As a consequence, its location detection is, at times, mixed with the tail information, and some tail-tip extraction is not always accurate. The 16:01:10 is a case illustrating the OV-10 having a large roll angle. The 16:02:11 case illustrates the airplane being covered by the time bar code.

Figures 14–17 illustrate the extracted depth for time windows of 15:17:52, 15:42:57, 16:01:10 and 16:02:11 hours respectively, of flight 558 for both the airplane and the wakes. A comparison of the two indicates the nature of the encounter, i.e., whether the airplane was above, below, or crossing the wakes. The real difference in altitude for the 15:42:57 hour data extraction is between 650 and 600 feet (Table 4). Figure 15 shows a consistent error extracting the real depth of about 20 feet, which, by Table 5 indicates parallax error of about one pixel. There was no GPS data available for the 15:17:52 hour at the time of data reduction, but the depth extraction illustrated in Fig. 14 averages around 850 feet with an error of 50 feet, which also corresponds to a parallax error of no more than a pixel. Extracted depth is not always smaller than the depth indicated by the GPS data, as demonstrated by Figs. 16 and 17. Inaccuracies are particularly high for the right wing depth extraction, with an average error of 50 feet, which corresponds to 2-3 pixels for 650 feet (Fig. 16) and 3-5 pixels for 550 feet (Fig 17). The other tips were detected with a better accuracy of about ± 20 and ± 30 feet, for Fig. 16 and Fig. 17 respectively. This error corresponds to a parallax detection error of about a pixel for the first and around two pixels for the second. In the 16:01:10 extraction, the roll angle is at times as high as 6.3°, which might explain part of the observed error. In the 16:02:11 extraction, part of the airplane is covered by the time bar code, which causes inaccurate data reduction for the left and right wings, as observed in Fig. 17.

Figures 11 and 18–21 illustrate the extracted wake x-location for time windows of 15:42:07, 15:17:52, 15:42:57, 16:01:10 and 16:02:11 hours respectively, in flight 558. With the exception if Fig. 18, these figures demonstrate the extraction of steady and parallel wakes. The perturbations in Fig. 18 are local, and do not obscure the general behavior of the wakes. The reduction process also enabled the observation of the sinusoidal behavior of the wakes in Figs. 11, 18, 19 and 21. The sinusoidal behavior is, at times, correlated with a change in the depth measurement. The wakes (x_o, y_o, z_o) location is measured relative to the left camera image plane location, which is set to $(x_i, y_i, 0)$ (Section 2.1). Therefore, wake behavior might be attributed to the OV-10 maneuvering, which shifts the image plane location relative to the wake, and not to the wakes behavior at the particular time sequence. Depth extraction for the wake is accurate to parallax detection error of less than a pixel in all cases. Consequently, this set of figures demonstrates the high accuracy of wake detection and stereo reduction.

Figures 22–25 illustrate the extracted wing span for the 15:17:52, 15:42:57, 16:01:10 and 16:02:11 hours time windows respectively, in flight 558. These figures demonstrate a consistent estimate of a wing span that is up to 10 feet shorter than the true wing span. The consistency in the estimate indicates a systematic error that might stem from a combination of the following: tip location detection error, inaccurate stereo reduction due to roll angles that are different from zero for the OV-10, and inaccurate estimation of the deflection angle for the Boeing 737 in flight. As mentioned before, error detection of 1-2 pixels in each wing, corresponds to accumulative detection error of 3-4 pixels, which, in turn, means an X displacement of 3-5 feet for a true depth of 500 feet, and 6-8 feet for a true depth of 1000 feet, consistent with the inaccuracy range demonstrated in Figs. 22–25.

6 SUMMARY

This report summarizes the stereo-video data reduction of wake vortices and an intercepting airplane. It presented the theory of stereo vision, and its implementation as a data reduction tool that extracts the trailing airplane and the wake locations. The extracted results are analyzed with respect to their reduction accuracy, and the process robustness and consistency. As demonstrated by this report, accurate results were obtained regardless of the signal-to-noise ratio, the wake/airplane orientation and position within the image plane, or the strength of the water-reflectance signal. The data reduction technique is accurate within a margin of 1-2 pixels, which is a reasonable level given the water reflection signal, and the unknown calibration factors that might have caused inaccuracies, such as the OV-10 roll angle or wing deflections. The combination of the data reduction files and the summary graphs, such as those illustrated in Figs. 14–

25, provides a powerful assessment tool of the processed data, and paves the way to further analysis and comparison with theoretical calculations.

Acknowledgment

This work was performed under NASA Langley Research Center Contract NAS1-20431. Special thanks to Dave Wolverton and Bill Seufzer of CSC for the digitization support and the VIPS maintenance.

References

[1] E. L. Hall, *Computer Image Processing and Recognition*, Academic Press, 1979.

[2] D. H. Ballard and C. M. Brown, *Computer Vision*, Prentice Hall, 1982.

[3] A. Rosenfeld and A. C. Kak, *Digital Picture Processing*, Vol. 2, Academic Press, 1982.

[4] D. Marr, *Vision*, W. H. Freeman and Company, 1982.

[5] B. A. Childers and W. L. Snow, "Video Photogramatic Considerations for Measuring the Proximity of a Probe Aircraft with a Smoke Seeded Trailing Vortex", *NASA TM 102691*, 1990.

[6] B. Stuever, E. C. Stewart and R. A. Rivers, "Overview of the Preparation and the Use of an OV-10 Aircraft for Wake Vortex Hazards Flight Experiment", *AIAA 95-3935*, 1995.

[7] D. Vicroy, J. Brandon G. Green, R. A. Rivers, G. Shah, E. C. Stewart and B. Stuever, "Characterizing the Hazard of a Wake Vortex Encounter", *AIAA 97-0055*, 1997.

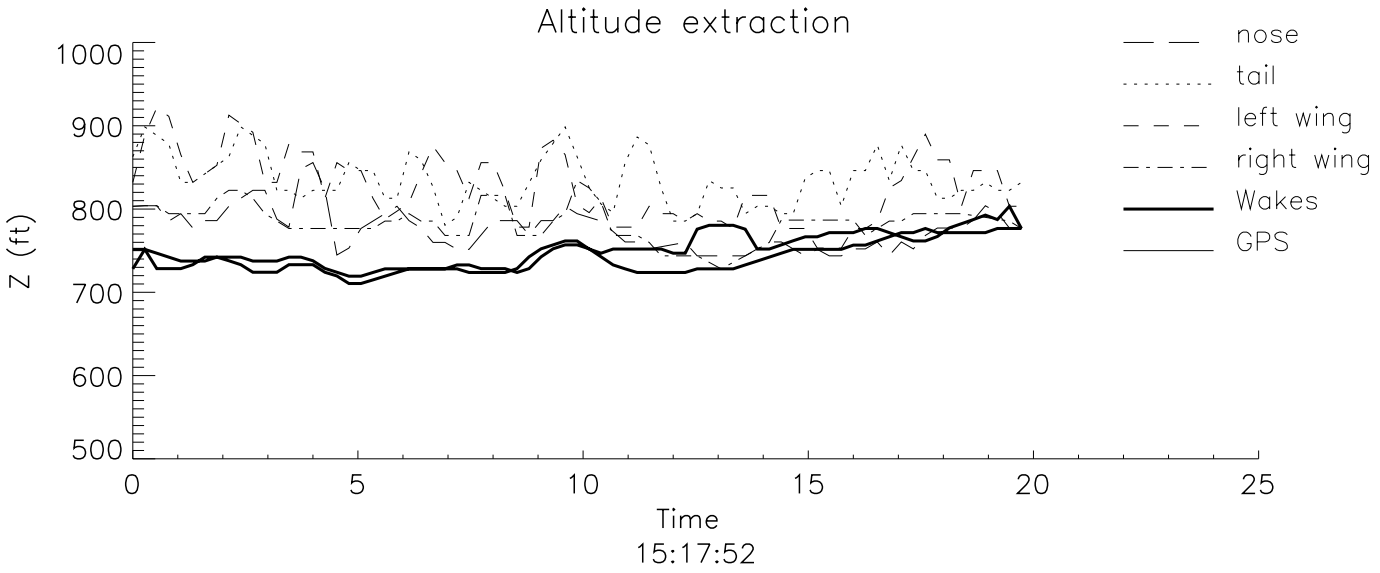

Figure 14: Measured altitude of the wakes and the airplane's four extracted tips, for flight 558, time window starting at 15:17:52.

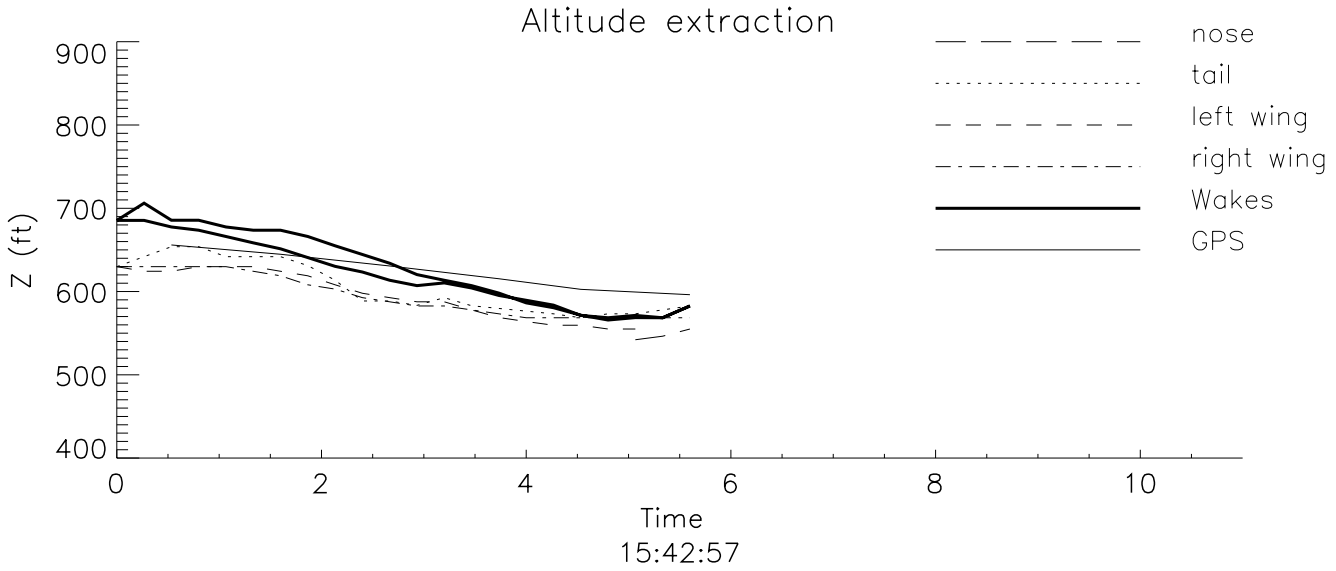

Figure 15: Measured altitude of the wakes and the airplane's four extracted tips, for flight 558, time window starting at 15:42:57.

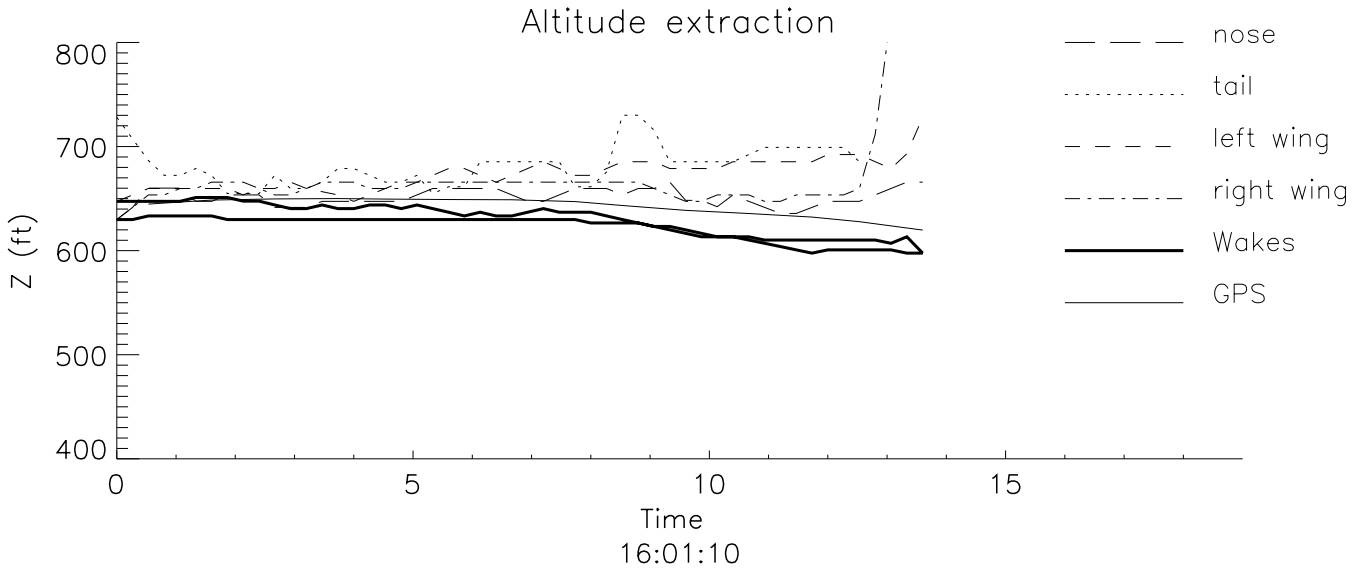

Figure 16: Measured altitude of the wakes and the airplane's four extracted tips, for flight 558, time window starting at 16:01:10.

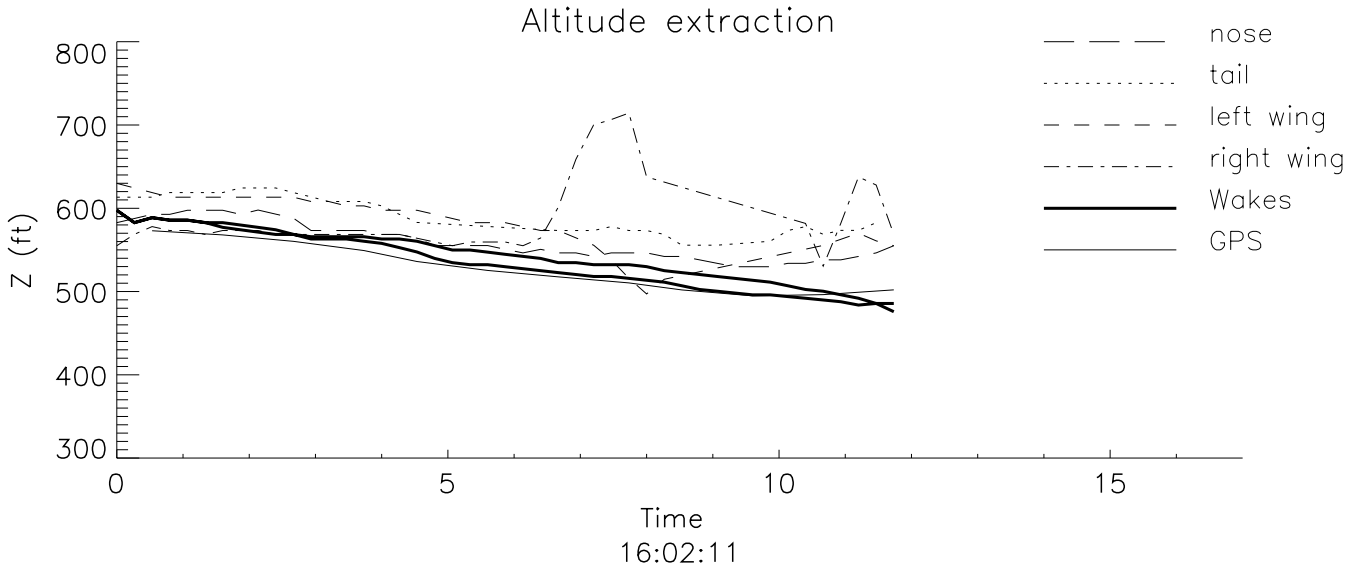

Figure 17: Measured altitude of the wakes and the airplane's four extracted tips, for flight 558, time window starting at 16:02:11.

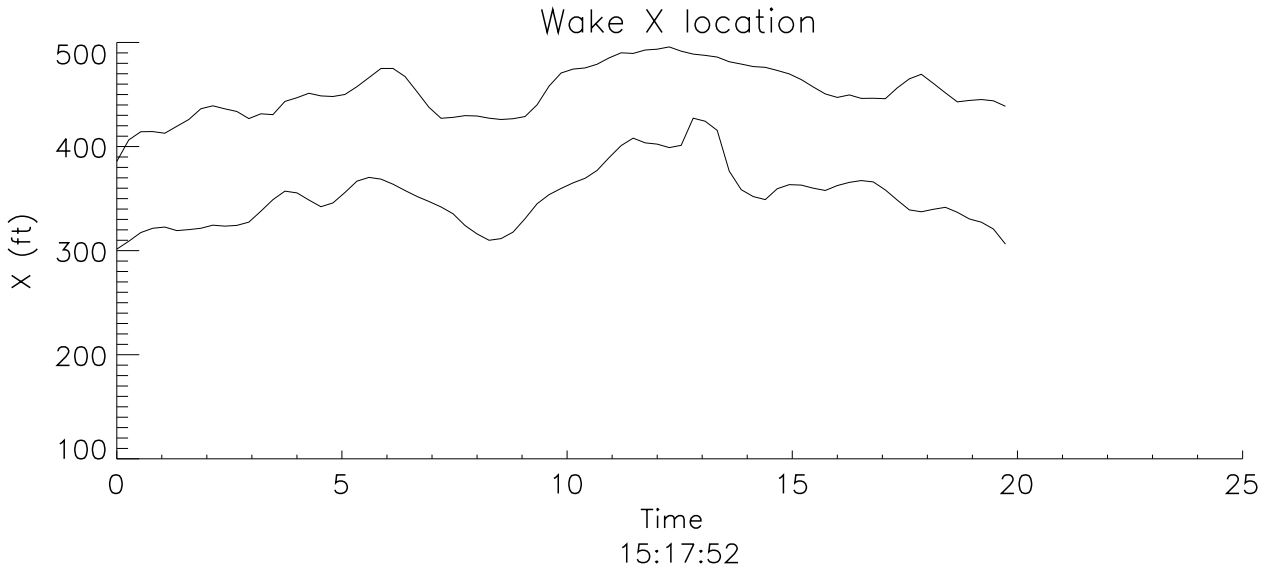

Figure 18: The wakes x-locations, as extracted from the stereo information for flight 558, time window starting at 15:17:52.

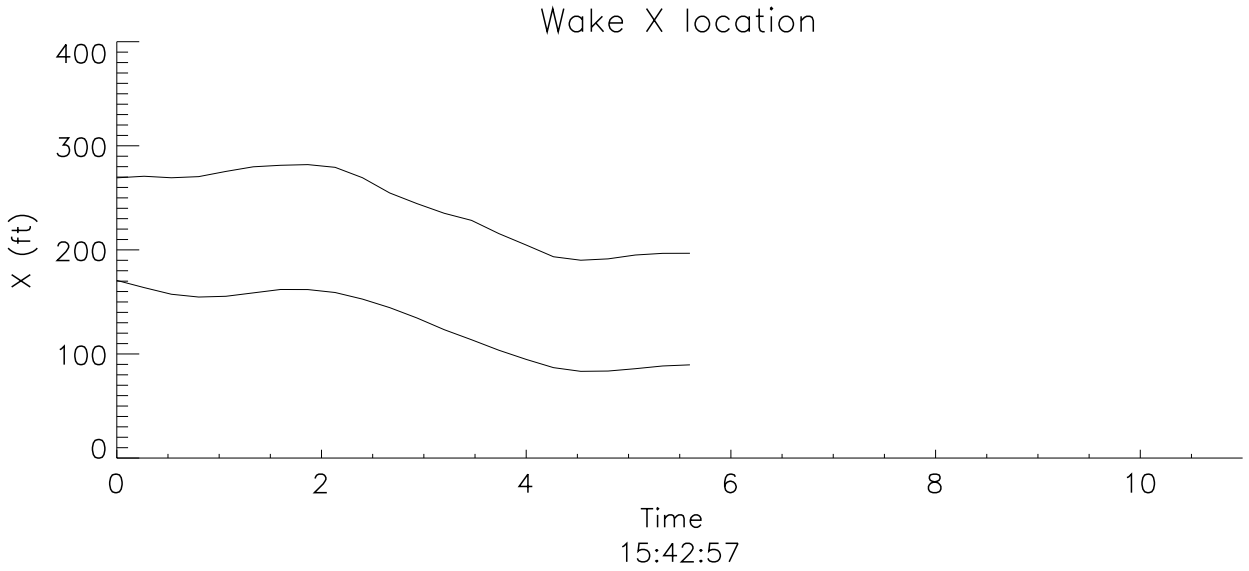

Figure 19: The wakes x-locations, as extracted from the stereo information for flight 558, time window starting at 15:42:57.

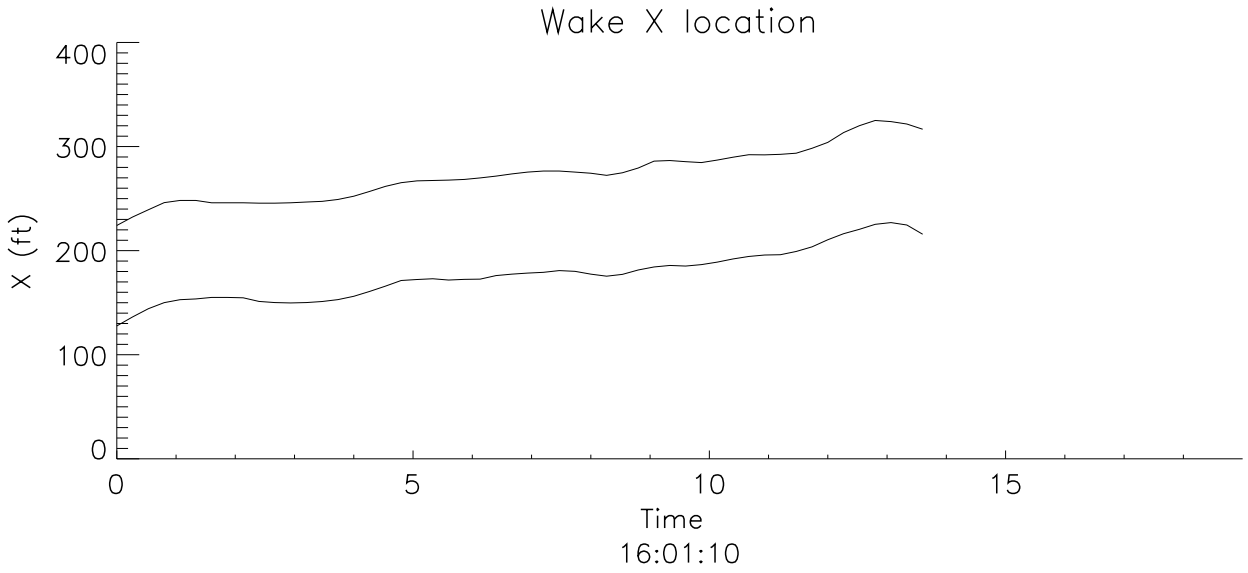

Figure 20: The wakes x-locations, as extracted from the stereo information for flight 558, time window starting at 16:01:10.

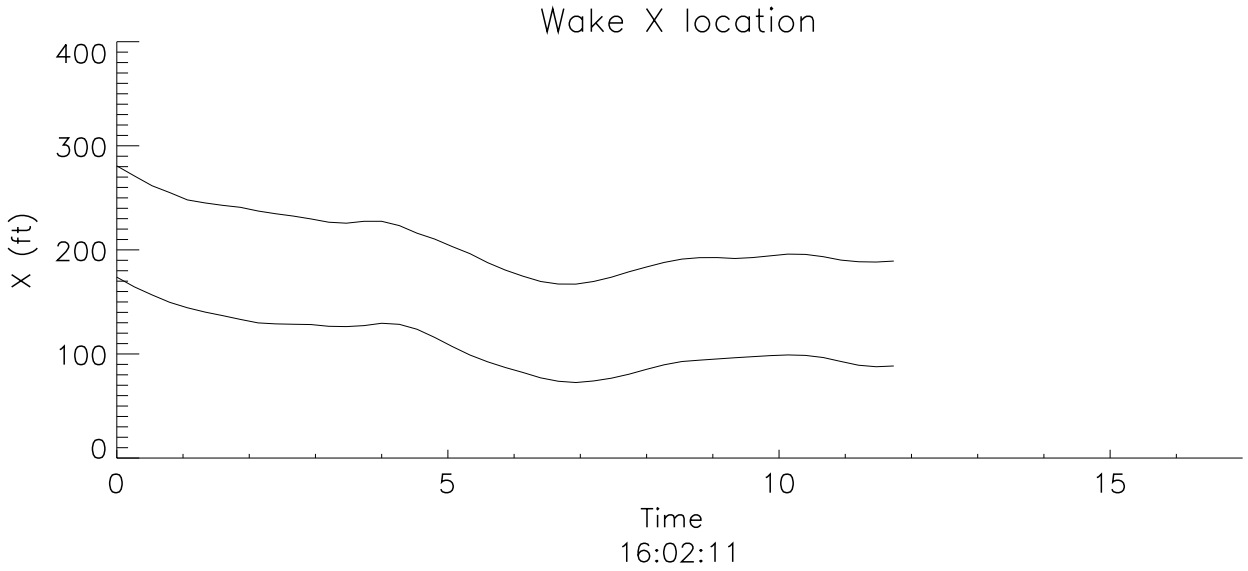

Figure 21: The wakes x-locations, as extracted from the stereo information for flight 558, time window starting at 16:02:11.

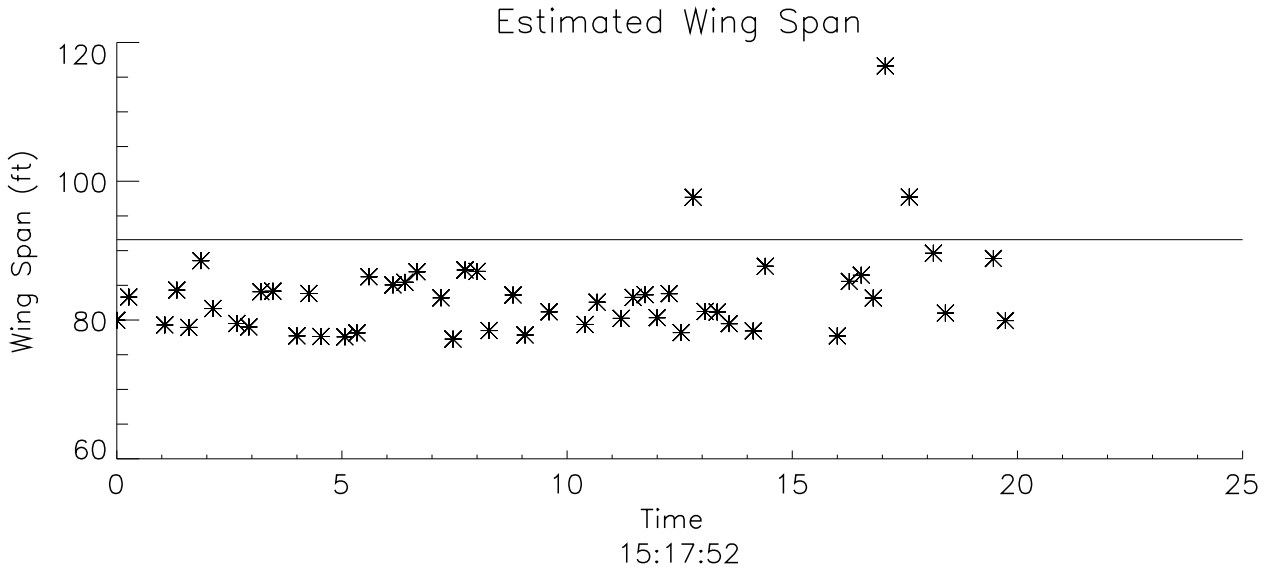

Figure 22: Wing-span estimate extracted from the distance between the wing tip locations. Flight 558, time window starting at 15:17:52.

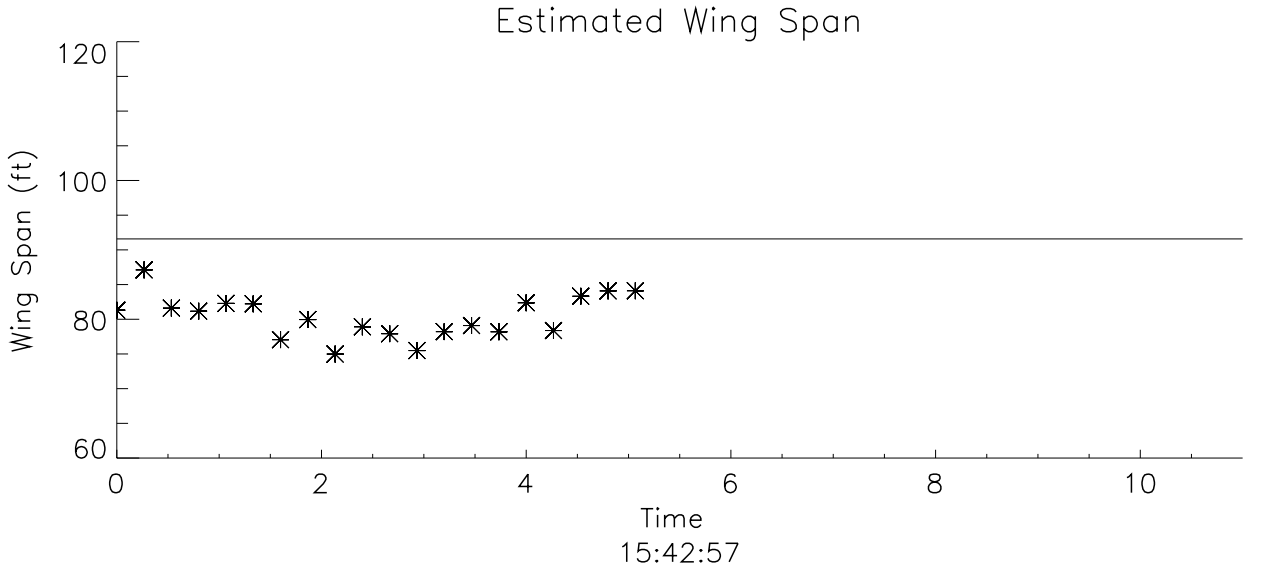

Figure 23: Wing-span estimate extracted from the distance between the wing tip locations. Flight 558, time window starting at 15:42:57.

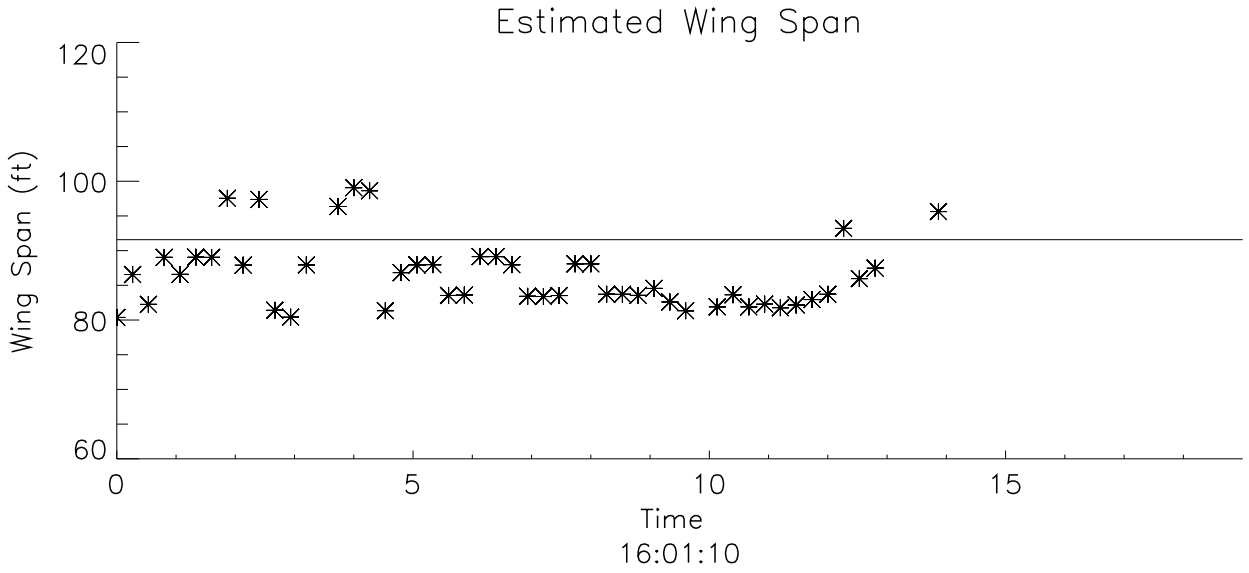

Figure 24: Wing-span estimate extracted from the distance between the wing tip locations. Flight 558, time window starting at 16:01:10.

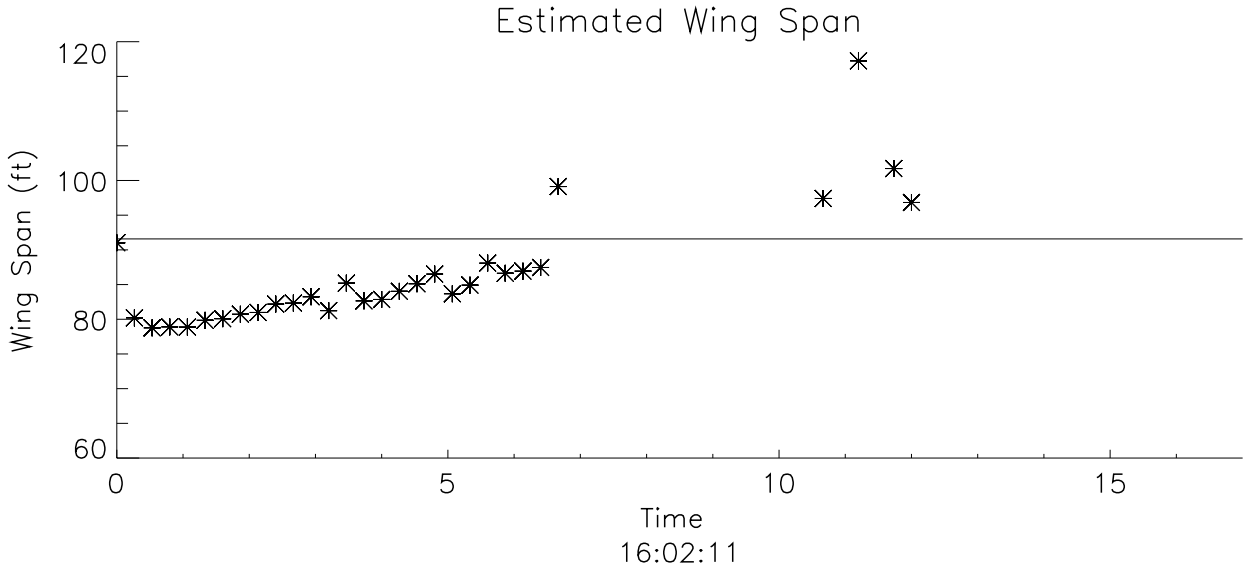

Figure 25: Wing-span estimate extracted from the distance between the wing tip locations. Flight 558, time window starting at 16:02:11.

REPORT DOCUMENTATION PAGE

Form Approved
OMB No. 0704-0188

Public reporting burden for this collection of information is estimated to average 1 hour per response, including the time for reviewing instructions, searching existing data sources, gathering and maintaining the data needed, and completing and reviewing the collection of information. Send comments regarding this burden estimate or any other aspect of this collection of information, including suggestions for reducing this burden, to Washington Headquarters Services, Directorate for Information Operations and Reports, 1215 Jefferson Davis Highway, Suite 1204, Arlington, VA 22202-4302, and to the Office of Management and Budget, Paperwork Reduction Project (0704-0188), Washington, DC 20503.

1. AGENCY USE ONLY (Leave blank)	2. REPORT DATE	3. REPORT TYPE AND DATES COVERED
	September 1998	Contractor Report

4. TITLE AND SUBTITLE
Stereo-Video Data Reduction of Wake Vortices and Trailing Aircrafts

5. FUNDING NUMBERS
NAS1-20431
WU 548-10-11-01

6. AUTHOR(S)
Rachel Alter-Gartenberg

7. PERFORMING ORGANIZATION NAME(S) AND ADDRESS(ES)
Computer Sciences Corp.
3217 N. Armistead Ave.
Hampton, VA 23666

8. PERFORMING ORGANIZATION REPORT NUMBER

9. SPONSORING/MONITORING AGENCY NAME(S) AND ADDRESS(ES)
National Aeronautics and Space Administration
Langley Research Center
Hampton, VA 23681-2199

10. SPONSORING/MONITORING AGENCY REPORT NUMBER
NASA/CR-1998-208719

11. SUPPLEMENTARY NOTES

12a. DISTRIBUTION/AVAILABILITY STATEMENT
Unclassified-Unlimited
Subject Category 61 Distribution: Standard
Availability: NASA CASI (301) 621-0390

12b. DISTRIBUTION CODE

13. ABSTRACT (Maximum 200 words)
This report presents stereo image theory and the corresponding image processing software developed to analyze stereo imaging data acquired for the wake-vortex hazard flight experiment conducted at NASA Langley Reseaerch Center. In this experiment, a leading Lockheed C-130 was equipped with wing-tip smokers to visualize its wing vortices, while a trailing Boeing 737 flew into the wake vortices of the leading airplane. A Rockwell OV-10A airplane, fitted with video cameras under its wings, flew at 400 to 1000 feet above and parallel to the wakes, and photographed the wake interception process for the purpose of determining the three-dimensional location of the trailing aircraft relative to the wake. The report establishes the image-processing tools developed to analyze the video flight-test data, identifies sources of potential inaccuracies, and assesses the quality of the resultant set of stereo data reduction.

14. SUBJECT TERMS	15. NUMBER OF PAGES
Stereo Vision, Image Processing, Wake Vertices, Wing-Tip Vortices, Visualization, In-Wake Flight	42
	16. PRICE CODE: A03

17. SECURITY CLASSIFICATION OF REPORT	18. SECURITY CLASSIFICATION OF THIS PAGE	19. SECURITY CLASSIFICATION OF ABSTRACT	20. LIMITATION OF ABSTRACT
Unclassified	Unclassified	Unclassified	